1-8-2014

Sea State Dependence of the Wind Stress Over the Ocean Under Hurricane Winds

Brandon G. Reichl

Tetsu Hara
University of Rhode Island, thara@uri.edu

Isaac Ginis
University of Rhode Island, iginis@uri.edu

Citation/Publisher Attribution
Reichl, B.G.; Hara, T.; Ginis, I. (2014). "Sea state dependence of the wind stress over the ocean under hurricane winds." Journal of Geophysical Research: Oceans. 119(1): 30-51. doi: 10.1002/2013JC009289
Available at: https://doi.org/10.1002/2013JC009289

JOURNAL OF GEOPHYSICAL RESEARCH: OCEANS, VOL. 119, 30–51, doi:10.1002/2013JC009289, 2014

Sea state dependence of the wind stress over the ocean under hurricane winds

Brandon G. Reichl,[1] Tetsu Hara,[1] and Isaac Ginis[1]

Received 19 July 2013; revised 8 November 2013; accepted 20 November 2013; published 8 January 2014.

[1] The impact of the surface wave field (sea state) on the wind stress over the ocean is investigated with fetch-dependent seas under uniform wind and with complex seas under idealized tropical cyclone winds. Two different approaches are employed to calculate the wind stress and the mean wind profile. The near-peak frequency range of the surface wave field is simulated using the WAVEWATCH III model. The high-frequency part of the surface wave field is empirically determined using a range of different tail levels. The results suggest that the drag coefficient magnitude is very sensitive to the spectral tail level but is not as sensitive to the drag coefficient calculation methods. The drag coefficients at 40 m/s vary from 1×10^{-3} to 4×10^{-3} depending on the saturation level. The misalignment angle between the wind stress vector and the wind vector is sensitive to the stress calculation method used. In particular, if the cross-wind swell is allowed to contribute to the wind stress, it tends to increase the misalignment angle. Our results predict enhanced sea state dependence of the drag coefficient for a fast moving tropical cyclone than for a slow moving storm or for simple fetch-dependent seas. This may be attributed to swell that is significantly misaligned with local wind.

Citation: Reichl, B. G., T. Hara, and I. Ginis (2014), Sea state dependence of the wind stress over the ocean under hurricane winds, *J. Geophys. Res. Oceans*, *119*, 30–51, doi:10.1002/2013JC009289.

1. Introduction

[2] The wind stress (or the drag coefficient) at the ocean surface is one of the most important parameters needed for ocean, atmosphere, and surface wave models. In particular, accurate predictions of tropical storm (hurricane) track and intensity require detailed knowledge of the spatial and temporal development of the wind stress that is strongly modified by complex surface wave fields (sea states).

[3] Many previous studies have investigated how the wind stress is modified by different sea states. They all start with the momentum conservation constraint that the wind stress is equal to the sum of the momentum flux into surfaces waves (form drag of surface waves) and the momentum flux directly into the subsurface currents (through viscous stress). The momentum flux into the waves is then expressed as an integral of the wave variance spectrum multiplied by the wave growth rate. Beyond this common basic framework, however, the studies significantly diverge in a few key aspects. These aspects include the parameterization of the high-frequency part (tail) of the wave variance spectrum, calculation of the wave growth rate due to wind, the feedback of the form drag due to waves on the mean wind profile, and wave breaking impacts.

[4] In order to estimate the sea state-dependent wind stress, a wave variance spectrum must be specified first. Often the wave variance spectrum is defined empirically. For example, several studies [*Makin and Kudryavtsev*, 1999; *Kudryavtsev and Makin*, 2001; *Makin and Kudryavtsev*, 2002; *Mueller and Veron*, 2009] used a wave spectrum based on the spectrum introduced by *Elfouhaily et al*. [1997]. This spectrum is a combination of a low-frequency model that is dependent on the wind speed and fetch, and a high-frequency model that is dependent on the wind friction velocity. The studies of *Kudryavtsev and Makin* [2001] and *Makin and Kudryavtsev* [2002] defined the high-frequency spectrum using the energy balance model proposed by *Kudryavtsev et al*. [1999]. The study of *Moon et al*. [2004b, hereinafter MGHBT] and *Donelan et al*. [2012, hereinafter DCCM] considered more complex sea states, including those under tropical cyclone winds, by explicitly simulating the wave variance spectrum. MGHBT modeled the wave variance spectrum using the WAVEWATCH III [*Tolman*, 2009] (hereinafter WW3) ocean wave model, while DCCM modeled the wave spectrum using the University of Miami wave model (UMWM). It is well known that the high-frequency part (tail) of the spectrum has a significant impact on the air-sea momentum flux. While the tail is included in the empirical parameterization of *Elfouhaily et al*. [1997], numerical wind-wave models typically resolve the spectrum to a certain frequency (not far from the spectral peak) and require empirical tail parameterizations to extend the spectrum to high

[1]Graduate School of Oceanography, University of Rhode Island, Narragansett, Rhode Island, USA.

Corresponding author: B. G. Reichl, Graduate School of Oceanography, University of Rhode Island, 215 S Ferry Rd., Narragansett, RI 02882, USA. (breichl@my.uri.edu)

2169-9275/14/10.1002/2013JC009289

frequencies. The study of MGHBT used the resolved spectrum up to $3 \times f_{pi}$ (f_{pi} is the peak input frequency, which is the peak frequency of the wind sea portion of the wave spectrum and is one of the standard outputs of the wave model) and then applied the equilibrium tail model developed by *Hara and Belcher* [2002]. DCCM resolved the spectrum to 2 Hz and extended the spectrum using an empirical relationship between the spectral slope of the tail and the wind speed.

[5] Once the spectrum is specified, the next step is to calculate the form drag using the wave growth rate. Previous studies parameterized the wave growth rate either using the wind speed [*Snyder et al*., 1981; *Donelan et al*., 2006; *Tsagareli et al*., 2010; DCCM] or the wind stress [after *Plant*, 1982]. The parameterizations with the wind stress are further divided into those using the total wind stress [*Janssen*, 1991], and those using the reduced stress, which accounts for the reduction of the wind forcing in the presence of larger-scale waves [e.g., *Makin and Mastenbroek*, 1996; *Makin and Kudryavtsev*, 1999; *Hara and Belcher*, 2004; *Mueller and Veron*, 2009; *Banner and Morison*, 2010; MGBHT]. One early study also considered a hybrid growth rate that is a function of both the full wind stress and wind speed [*Makin et al*., 1995]. Another unresolved aspect of the growth rate is the impact of swell that may or may not be aligned with the local wind. Observational evidences show that the wind stress may be modulated by the presence of swell [e.g., *Donelan et al*., 1997; *Drennan et al*., 1999; *Grachev et al*., 2003; *García-Nava et al*., 2009, 2012]. DCCM explicitly included the impact of swell on the form drag calculation by considering different growth rates for waves that are faster than or opposite to the wind. MGHBT neglected the impact of swell on the growth rate.

[6] The final step of the drag coefficient calculation is to model the feedback of the form drag of waves on the mean wind profile. This step is needed to establish a relationship between the wind stress and the wind speed (normally at 10 m height). The neutral wind profile in some studies is simply approximated using log-layer vertical wind profiles [e.g., *Kudryavtsev and Makin*, 2001; *Mueller and Veron*, 2009; DCCM]. In this case, the wind profile is dependent only on the surface roughness parameter, z_0, that is, the feedback appears only in the parameterization of the sea state-dependent z_0. Other studies account for the feedback of the modified turbulent stress (due to form drag) on the mean wind shear in the wave boundary layer using various turbulence closure methods [e.g., *Makin and Mastenbroek*, 1996; *Makin and Kudryavtsev*, 1999; *Hara and Belcher*, 2004; MGHBT]. Some studies [*Hara and Belcher*, 2004; MGHBT] explicitly ensure that energy remains conserved in the wave boundary layer.

[7] When surface waves break, the airflow may separate at the wave crest and apply increased form drag on the waves. While earlier studies did not explicitly account for the impact of breaking waves on the form drag [e.g., *Makin and Kudryavtsev*, 1999; MGHBT], many recent studies separated the form drag of breaking waves from the form drag of nonbreaking waves [*Kudryavtsev and Makin*, 2001; *Kudryavtsev et al*., 2001; *Makin and Kudryavtsev*, 2002; *Kukulka and Hara*, 2008a, 2008b; *Mueller and Veron*, 2009; *Banner and Morison*, 2010]. The inclusion of an explicit breaking-wave component into a wind stress model introduces additional complexities and uncertainties into the wind stress model. First, the presence of breaking waves is often represented by a breaking-wave distribution. This distribution is not well known and often parameterized from the spectrum and the growth rate [*Kudryavtsev and Makin*, 2001; *Makin and Kudryavtsev*, 2002; *Mueller and Veron*, 2009]. Second, the momentum exchange between breaking waves and the wind must be modeled. This is often simplified by assuming that the shape of the wave can be approximated as a backward facing step where the airflow separates [*Kudryavtsev and Makin*, 2001; *Makin and Kudryavtsev*, 2002; *Kukulka and Hara*, 2008a, 2008b; *Mueller and Veron*, 2009]. Third, the feedback of the breaking and nonbreaking form drag on the mean wind profile needs to be included.

[8] *Kukulka and Hara* [2008a, 2008b] included the breaking-wave effect on the drag coefficient over a wide range of sea states from laboratory conditions to open ocean conditions. They allowed large uncertainties in the breaking distribution, the form drag of breaking waves, as well as the wave spectrum at high frequencies (tail) that is limited by wave breaking. They found that in open ocean conditions the most significant breaking-wave impact on the drag coefficient appears in reducing the level of the spectral tail rather than in enhancing the form drag due to flow separation. This is because the occurrence of dominant-scale breaking waves is relatively rare in the open ocean. (In contrast, the dominant-scale breakers determine the drag coefficient in laboratories, since almost all dominant waves break.) An alternative (simpler) approach to implicitly including the breaking-wave effect is to define the average growth rate of all waves (including nonbreaking and breaking waves). In fact, the study of DCCM tuned their growth rate to observations that included both breaking and nonbreaking conditions.

[9] In summary, the impact of different sea states on the wind stress is still an unresolved question, particularly with complex wave fields such as those under tropical cyclone winds. The main objective of this study is to investigate the effect of different sea states on the wind stress with the help of numerical experiments. We will conduct two types of experiments. The first type will be fetch-dependent simulations under constant uniform winds. The second type will use idealized tropical cyclone wind fields to force simulations of the waves. We will evaluate two distinct approaches of estimating the momentum flux, one proposed by DCCM and the other based on MGHBT, using identical wave spectra. We seek to determine to what degree the estimations of the wind stress depend on different assumptions regarding the two key aspects: wave growth rate and feedback on the wind profile. Furthermore, we will investigate the impact of the different spectral tail parameterizations and examine misalignment between the wind stress vector and the wind speed vector in hurricane conditions.

2. Methods

2.1. Wave Spectrum Simulations

[10] In order to investigate the sea state-dependent wind stress, we first specify the wave spectrum. In this study, all wave spectra are simulated using the wind-wave model, WW3. WW3 is a third-generation model maintained by the

National Oceanic and Atmospheric Administration (NOAA) through the National Center for Environmental Prediction's (NCEP) Environmental Modeling Center (EMC). The latest operational model version, 3.14, is used in the simulations. The model accepts the 10 m wind speed (in time and in space) as an input, and calculates the wind stress using its own drag coefficient parameterization. It then calculates the wind forcing using its own wave growth rate parameterization. In principle, this WW3 growth rate should be consistent with the growth rate we use in our calculation of the sea state-dependent momentum flux, and the WW3 drag coefficient should be consistent with our own estimates as well. However, the WW3 drag coefficient and the growth rate have been empirically adjusted (together with the wave dissipation parameterization) to produce wave spectra that are consistent with observations, mainly in low to moderate wind conditions. It has been known that the model tends to overestimate the significant wave height in tropical cyclone conditions. Recently, *Fan et al*. [2009] have shown that the WW3 wave prediction significantly improves if the WW3 drag coefficient is replaced by the parameterization developed in *Moon et al*. [2004b, 2004a], which yields a lower drag coefficient at high wind speeds. In their study, the WW3 results were directly compared to Scanning Radar Altimeter (SRA) observations, and it was shown that the model accurately reproduced large variability of the significant wave height under complex hurricane wind conditions. We therefore employ the same drag coefficient as in *Fan et al*. [2009] for the wave simulations in this study. However, the feedback of the sea state-dependent drag coefficient obtained in this study on surface wave simulations is not pursued here. For a complete description of WW3 including the governing equations see *Tolman* [2009].

[11] WW3 explicitly simulates waves up to 3× the peak input frequency. Internally the model attaches a spectral tail that is highly sea state dependent. This parameterized tail is largely a residual of the tuning process and has not been thoroughly validated against observations (H. Tolman, personal communication, 2012). The dependences of the spectral tail level on the wind speed and the wave age ($c_p/u_\star$, where c_p is the phase speed at the spectral peak and $u_\star$ is the wind friction velocity) are still poorly understood, because very few direct observations exist. Since the stress calculation is very sensitive to the tail level, we need to parameterize the tail level and investigate its impact on the drag coefficient calculation.

[12] There are few observation of the spectral level of the tail in the field. Observations by *Romero and Melville* [2010] in the Gulf of Tehuantepec showed that the directionally integrated saturation spectrum ($B(k)=\Psi(k)\times k^4$, where $\Psi(k)=\int_{-\pi}^{\pi}\Psi(k,\theta)d\theta$, and the directional wave number spectrum $\Psi(k,\theta)$ is defined such that the mean square surface displacement is equal to $\int_{-\pi}^{\pi}\int_0^{\infty}\Psi(k,\theta)kdkd\theta$) in the tail is roughly independent of k and falls between 6×10^{-3} and 10×10^{-3} for wind speeds between 11 and 20 m/s and wave ages between 17 and 32. Their results were roughly consistent with previous findings over similar wave numbers [*Forristall*, 1981; *Banner et al*., 1989]. They did not find a significant wave age dependence of the tail level within the range of their observations. Note that their data were collected under a gap flow and the resulting wave field may be different from typical ocean conditions. In higher wind conditions, there are no reliable observations of the tail levels.

[13] Since our knowledge of the spectral tail is very limited, particularly at high wind conditions, we will test a wide range of B values and investigate its impact on the drag coefficient. Since there is no consensus regarding the dependence of the tail on the wind speed or wave age, we set the saturation spectrum B in the tail as constant in k and with no systematic variation with the wave age or wind speed in each experiment. We will simulate the peak region of the wave spectrum using WW3, and smoothly transition the result to the parameterized tail at high frequencies. Specifically, the WW3 spectrum is used up to 1.25 × the peak input frequency. From 1.25 × to 3 × the peak input frequency the spectrum is linearly varied from the explicit model calculation to the predetermined B value. The spreading function is also changed from the explicit calculation result to simple cosine squared dependence around the direction of the near-surface wind vector.

[14] In our preliminary analysis, it became apparent that any single B value for the tail does not reproduce the value of the drag coefficient given by the COARE 3.5 air-sea flux parameterizations at its full range of wind speeds [*Edson et al*., 2013], suggesting that the tail level systematically increases with wind speed between 0 and 20 m/s. The COARE 3.5 is a recent and comprehensive drag coefficient parameterization and is therefore chosen as a benchmark to compare our results to. (We also include comparisons to the classic *Large and Pond* [1981] drag coefficient parameterization for reference.) We therefore vary the B values over a sufficiently large range such that our models can reproduce the observed drag coefficient in all wind speeds up to 20 m/s. Specifically, we will test three different values; the low B value ($B=2\times10^{-3}$) yields better agreement with the drag coefficient of the COARE 3.5 algorithm at 5 m/s, the medium B value ($B=6\times10^{-3}$) shows better agreement with the COARE 3.5 at 10 m/s, and the high B value ($B=12\times10^{-3}$) shows a better agreement at 20 m/s. This range of B values encompasses the variability reported in the observations [*Forristall*, 1981; *Banner et al*., 1989; *Romero and Melville*, 2010]. It is certainly possible that B may become either greater than 12×10^{-3} at higher wind speeds and/or at very young seas or less than 2×10^{-3} under lower wind speeds. Nevertheless our choice of the three different B values is sufficiently broad to systematically study the impact of the tail on the drag coefficient.

[15] Directionally integrated saturation spectra for two wind speeds at a fetch of 100 km (the experimental set up is presented in the next section) are shown to demonstrate the transition from the WW3 spectrum to the three parameterized tail levels (Figure 1). Note that at high winds the WW3 tail parameterization is higher than even the highest of our three tail levels. The empirical spectrum of *Elfouhaily et al*. [1997] is also shown in the figure for reference. While their spectrum is very high for the gravity-capillary waves at high wind speeds, their saturation spectrum of the short gravity waves (k up to 50 rad/m or so) is within the range of our investigation. In this study, we do not account for the enhancement of B in the gravity-capillary range and simply truncate the spectrum at a fixed wave number $k = 400$ rad/m for simplicity. The impact of

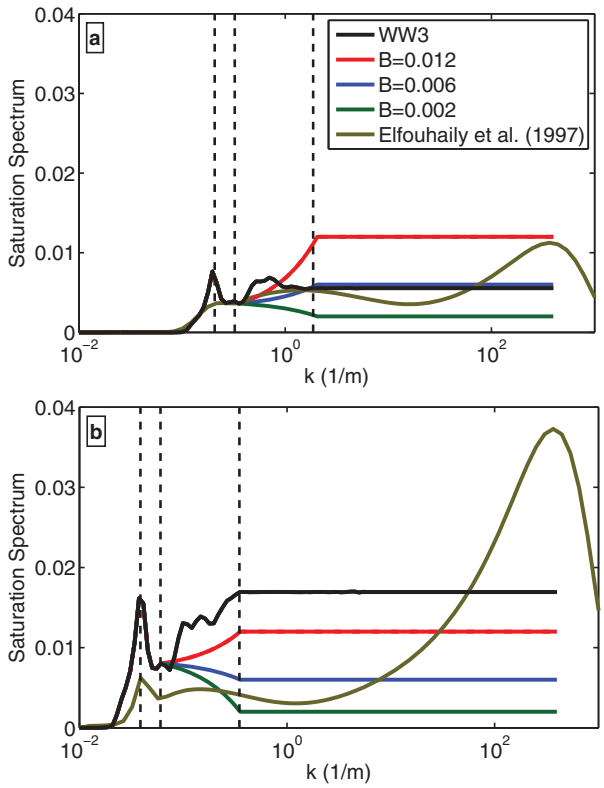

Figure 1. Directionally integrated saturation spectrum with the peak of the wave field simulated in WW3. The first dashed vertical line (left to right) represents the peak input frequency, the second is 1.25 × the peak input frequency, and the third line is 3 × the peak input frequency. The original WW3 spectrum, *Elfouhaily et al.*'s [1997] empirical spectrum, and the three tail level options tested during this experiment are plotted. The fetch is 100 km and the wind speed is (a) 10 m/s and (b) 40 m/s.

the spectral enhancement in the gravity-capillary range and a different cutoff wave number on our drag coefficient calculation is relatively small compared to the large variation of the tail level examined.

[16] To confirm that our choice of the B value range is reasonable, it is useful to examine the resulting mean square slope. In Figure 2, the calculated mean square slope from our fetch-dependent wave spectra (WW3 spectra with the three levels of the tail) at different wind speeds are shown. It is clear from this exercise that the mean square slope has a strong dependence on the tail level. To reproduce the mean square slope measured by *Cox and Munk* [1954], it is clear that the B value would need to increase from about 4×10^{-3} at 5 m/s to nearly 12×10^{-3} at 15 m/s. It is interesting that these B values are quite consistent with the B values that yield drag coefficients similar to the COARE 3.5 algorithm. At higher wind speeds the mean square slope given by a linear extrapolation of the *Cox and Munk* [1954] is much higher than that calculated using our highest tail. This suggests that we have either underestimated the B value at high winds, or that the *Cox and Munk* [1954] relationship does not apply well to higher winds. Unfortunately, we cannot validate/invalidate our mean square slope estimates at higher wind speeds because no direct observations exist.

2.2. Calculation of the Air-Sea Momentum Flux, Mean Wind Profile, and Drag Coefficient

[17] As discussed earlier, in this study, we apply two different approaches to estimate the momentum flux and drag coefficient using identical wave spectra. The first approach is identical to that proposed by DCCM. The second approach (denoted by RHG hereafter) is based on MGHBT but has been modified to account for the effect of swell and to allow different parameterized tail levels. In both approaches the momentum flux from the atmosphere to the ocean is calculated from a momentum conservation constraint. To the leading order, the momentum flux at the surface is a sum of the viscous stress, τ_v, and the form stress, τ_f.

$$\tau=\tau_v+\tau_f \tag{1}$$

[18] The form stress at the surface includes the impact of all waves and can be written:

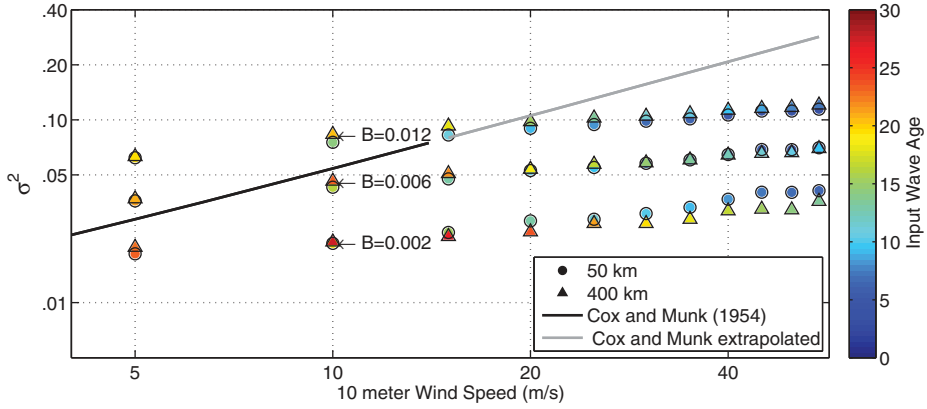

Figure 2. Mean square slope with the three different tail level options. The empirical linear relationships of *Cox and Munk* [1954] are plotted for reference up to wind speed 15 m/s (black), and are extrapolated to 55 m/s (gray). At each wind speed, the upper two data points are from the B = 0.012 tail, the middle two data points are from the B = 0.006 tail, and the lower two data points are from the B = 0.002 tail.

$$\boldsymbol{\tau}_f = \rho_w \int_{k_{min}}^{k_{max}} \beta_g(k,\theta)\sigma\Psi(k,\theta)d\theta\mathbf{k}dk \tag{2}$$

where ρ_w is the water density, k is the wave number, θ is the wave direction, σ is the angular frequency, $\beta_g(k,\theta)$ is the growth rate, $\Psi(k,\theta)$ is the wave variance spectrum, and k_{min} and k_{max} are the minimum and maximum wave numbers of contributing waves.

[19] In DCCM the growth rate is expressed as a function of the wind speed.

$$\beta_g(k,\theta) = A_1\sigma\frac{\left[u_{\lambda/2}\cos(\theta-\theta_w)-c\right]\left|u_{\lambda/2}cos(\theta-\theta_w)-c\right|}{c^2}\frac{\rho_a}{\rho_w} \tag{3}$$

$$A_1 = \begin{cases} 0.11, & : u_{\lambda/2}\cos\theta > c, \quad \text{for wind forced sea} \\ 0.01 & : 0 < u_{\lambda/2}\cos\theta < c, \quad \text{for swell faster than the wind} \\ 0.1 & : \cos\theta < 0, \quad \text{for swell opposing the wind} \end{cases} \tag{4}$$

where A_1 is the proportionality coefficient determined empirically (so that modeled wave spectra agree with field observations), $u_{\lambda/2}$ is the wind speed at the height of half the wavelength (up to 20 m), θ_w is the wind direction, and c is the wave phase speed. Note that the wind velocity should be taken relative to the current velocity.

[20] The wind speed is calculated using the law of the wall for rough surfaces

$$u(z) = \frac{u_\star}{\kappa}\ln\left(\frac{z}{z_0}\right) \tag{5}$$

where κ is the von Kármán coefficient.

[21] The viscous stress is calculated from the law of the wall for smooth surfaces. The viscous drag coefficient, Cd_v is adjusted to account for sheltering:

$$Cd'_v = \frac{Cd_v}{3}\left(1+\frac{2Cd_v}{Cd_v+Cd_f}\right) \tag{6}$$

where Cd_f is the form drag coefficient.

[22] The viscous stress can then be solved for as:

$$\boldsymbol{\tau}_v = \rho_a Cd'_v|\mathbf{u_z}|\mathbf{u}_z \tag{7}$$

[23] In RHG, the growth rate is calculated from the wind stress as in MGHBT. In this theory, the total stress is given as a function of height as:

$$\boldsymbol{\tau} = \boldsymbol{\tau}_t(z) + \boldsymbol{\tau}_f(z) \tag{8}$$

where τ_t is the turbulent stress and is equal to the viscous stress very near the surface. The form stress can be expressed as

$$\boldsymbol{\tau}_f(z) = \rho_w \int_{k_{min}}^{k=\delta/z}\int_{-\pi}^{\pi} \beta_g(k,\theta)\sigma\Psi(k,\theta)d\theta\mathbf{k}dk \tag{9}$$

that is, the form stress at height z is equal to the integration of the form stress at the surface for wave numbers below $k=\delta/z$, where δ/k is the inner layer height [*Hara and Belcher*, 2004] for waves at a wave number k. This expression is derived by assuming that the wave-induced stress is significant from the surface up to the inner layer height, but is negligible further above. Since at the surface

$$\boldsymbol{\tau} = \boldsymbol{\tau}_v + \boldsymbol{\tau}_f(z=0) = \boldsymbol{\tau}_v + \rho_w \int_{k_{min}}^{k_{max}}\int_{-\pi}^{\pi} \beta_g(k,\theta)\sigma\Psi(k,\theta)d\theta\mathbf{k}dk \tag{10}$$

the turbulent stress at a height z can be expressed as:

$$\boldsymbol{\tau}_t(z) = \boldsymbol{\tau}_v + \rho_w \int_{k=\delta/z}^{k_{max}}\int_{-\pi}^{\pi} \beta_g(k,\theta)\sigma\Psi(k,\theta)d\theta\mathbf{k}dk \tag{11}$$

[24] It is assumed that the turbulent stress at the inner layer height $z=\delta/k$ determines the growth rate of waves at wave number k:

$$\beta_g(k,\theta) = c_\beta\sigma\frac{|\tau_t(z=\delta/k)|}{\rho_w c^2}\cos^2(\theta-\theta_\tau) \tag{12}$$

where θ_τ is the direction of the turbulent stress at the inner layer height. The turbulent stress at the inner layer height is used in place of the total wind stress because longer waves reduce the effective wind forcing on shorter waves.

[25] In MGHBT, the effect of swell (slower waves and waves opposing wind) was simply ignored and the growth rate coefficient c_β was set as:

$$c_\beta = \begin{cases} 32 & : \cos(\theta-\theta_w) > 0 \quad \text{and} \quad c/u_\star^l < 1/0.07 \\ 0 & : \text{otherwise} \end{cases} \tag{13}$$

[26] In this study (RHG), c_β is modified to explicitly account for the swell:

$$c_\beta = \begin{cases} 25 & : \cos(\theta-\theta_w) > 0 \quad : c/u_\star^l < 10 \\ 10+15\cos[\pi(c/u_\star-10)/15] & : \quad : 10 \le c/u_\star^l < 25 \\ -5 & : \quad : 25 \le c/u_\star^l \\ -25 & : \cos(\theta-\theta_w) < 0 \end{cases} \tag{14}$$

[27] The growth rate coefficient c_β varies depending on the ratio of the wave phase speed to the local turbulent friction velocity (friction velocity at the inner layer height), $u_\star^l = \sqrt{\tau_t(z=\delta/k)/\rho_a)}$. As in DCCM, we define three regimes. When the wind stress direction and wave direction are within 90° of each other, we distinguish the wind forced waves ($c/u_\star^l < 10$) and the swell forcing wind ($c/u_\star^l > 25$). When wind opposes swell (wind stress direction and wave direction is misaligned by more than 90°), we assume strong wave dissipation and a large form drag as in DCCM. However, since the impact of opposing wind is not well understood, we will also test weaker forcing of opposing wind in Appendix B. Finally, between the wind forced wave regime and the swell forcing wind regime, we introduce a transition regime ($10 < c/u_\star^l < 25$) with a smoothly varying c_β that compares well to the data presented in *Belcher* [1999].

[28] In DCCM, the mean wind profile is assumed to be logarithmic, that is, the feedback of the waves appears only in the modified effective roughness length. In RHG, the

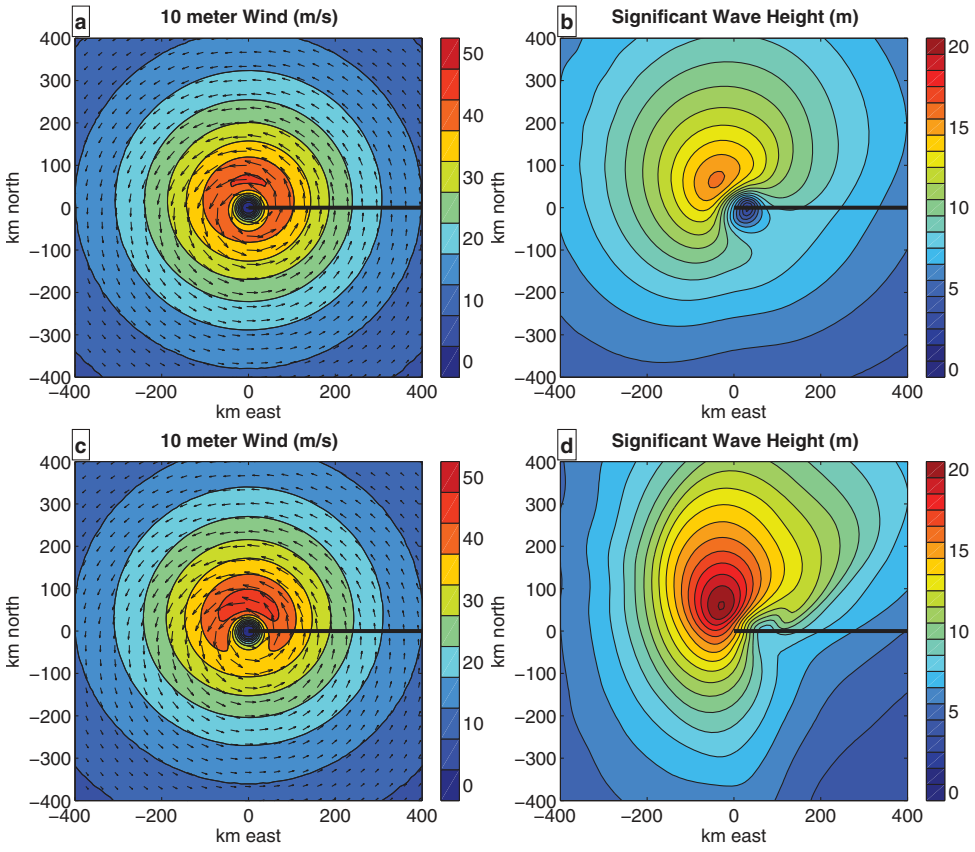

Figure 3. Wind used in the experiment and resulting wave field. (a and b) The upper plots are for a 5 m/s translating tropical cyclone while (c and d) the lower plots are for a 10 m/s translating tropical cyclone. Wind vectors are superimposed in the wind contour plots. The thick black line represents the track of the tropical cyclone through the domain.

wind profile is explicitly calculated using the energy conservation constraint in the wave boundary layer following MGHBT. From the top of the viscous sublayer to the inner layer height of the shortest waves, the wind shear is expressed as:

$$\frac{d\mathbf{u}}{\partial z} = \frac{\rho_a}{\kappa z}\left|\frac{\boldsymbol{\tau}_v}{\rho_a}\right|^{3/2} \frac{\boldsymbol{\tau}_v}{\boldsymbol{\tau}_v \cdot \boldsymbol{\tau}_{tot}} \quad \text{for} \quad z_v < z < \delta/k_l \tag{15}$$

[29] Between the inner layer height of the shortest waves and that of the longest waves the wind shear is expressed as:

$$\frac{d\mathbf{u}}{\partial z} = \left[\frac{\delta}{z^2}\tilde{F}_w\left(k=\frac{\delta}{z}\right) + \frac{\rho_a}{\kappa z}\left|\frac{\boldsymbol{\tau}_t(z)}{\rho_a}\right|^{3/2}\right] \times \frac{\boldsymbol{\tau}_t(z)}{\boldsymbol{\tau}_t(z) \cdot \boldsymbol{\tau}_{tot}} \quad \text{for} \quad \delta/k_l \le z \tag{16}$$

where $\tilde{F}_w(k=\delta/z)$ is the energy uptake by surface waves:

$$\tilde{F}_w(k=\delta/z) = \rho_w \int_{-\pi}^{\pi} \beta_g(k,\theta) g \Psi(k,\theta) k d\theta \tag{17}$$

[30] Finally, above the inner layer height of the longest waves the wave effect is negligible and the wind shear is aligned in the direction of the wind stress:

$$\frac{d\mathbf{u}}{dz} = \frac{u_\star}{\kappa z}\frac{\boldsymbol{\tau}_{tot}}{|\boldsymbol{\tau}_{tot}|} \tag{18}$$

[31] Although the inner layer height parameter δ is estimated to be around 0.05–0.1 [*Hara and Belcher*, 2004], its exact value is not known. In MGHBT, this parameter δ was effectively treated as a tuning parameter and its value was determined to match the resulting drag coefficient at low to medium wind speeds with existing empirical parameterizations. In this study, we also determine δ in the same empirical manner and set $\delta = 0.03$. Note that there are some uncertainties in the value of the growth parameter c_β as well. If the value of c_β is changed from those in (14), the value of δ needs to be modified to obtain similar drag coefficient values.

[32] Let us summarize the major differences between DCCM and RHG. One major difference that has already been mentioned is the calculation of the growth rate. DCCM parameterizes the growth rate from the wind speed, and RHG parameterizes the growth rate from the wind stress. Another more subtle difference is the directional dependence of the growth rate. The method of DCCM takes the projection of the wind in the direction of the waves and uses the difference between the two values to calculate the growth rate. This means waves propagating perpendicular

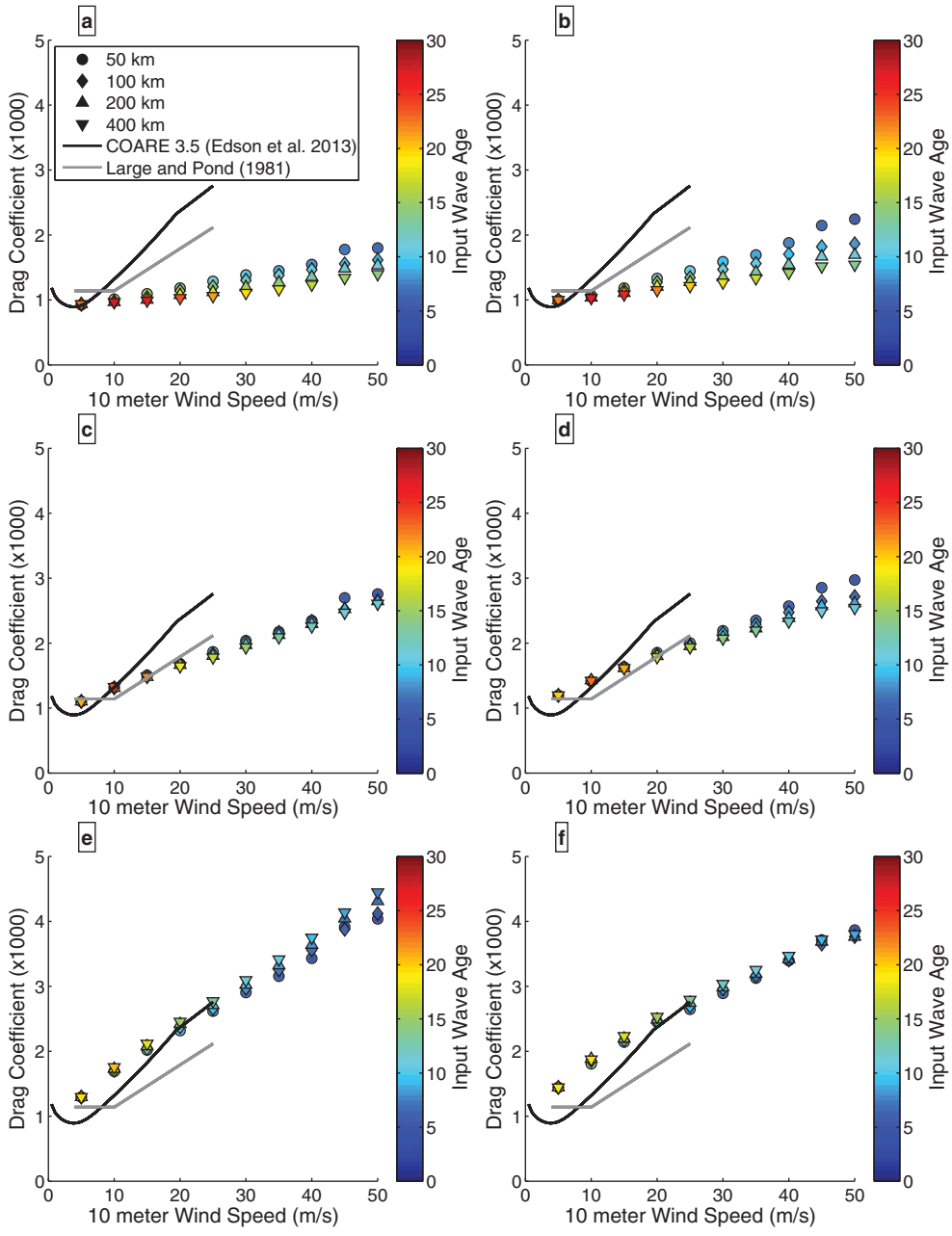

Figure 4. Drag coefficients (× 1000) for fetch-dependent simulations using three tail levels. Eleven simulations were conducted from wind speed 5–50 m/s. (a, c, and e) The left column is calculated using the RHG method, while (b, d, and f) the right column is calculated using the DCCM method. The saturation level is B = 0.002 (Figures 4a and 4b), B = 0.006 (Figures 4c and 4d), and B = 0.012 (Figures 4e and 4f).

($\pm 90^{\circ}$) to the wind will have an impact on the wind stress calculation because the phase speed of the waves is not 0. This is quite different from the method of RHG where the cosine squared of the angle between waves and wind stress is used to determine the growth rate. This value is 0 for waves propagating perpendicular to the wind. The impact of fast propagating swell misaligned at 90° to the wind is very different between the two models. Note that the value of A_1 in the DCCM model varies from 0.01 to 0.1 as the angle difference between wind and waves exceed 90°. Therefore, swell misaligned with wind by slightly more than 90° has a large impact on the wind stress calculation; such waves are particularly effective in increasing the misalignment between the wind stress direction and the wind speed direction as demonstrated later.

[33] The breaking wave impacts on the form drag are not explicitly calculated in either of the theories. In RHG, it is assumed that the breaking form drag of peak waves is not of the leading order [after *Kukulka and Hara*, 2008a]. The breaking effect is implicitly included in the high-frequency tail because the saturation spectrum value (B) is likely limited by wave breaking process. Furthermore, if the form drag

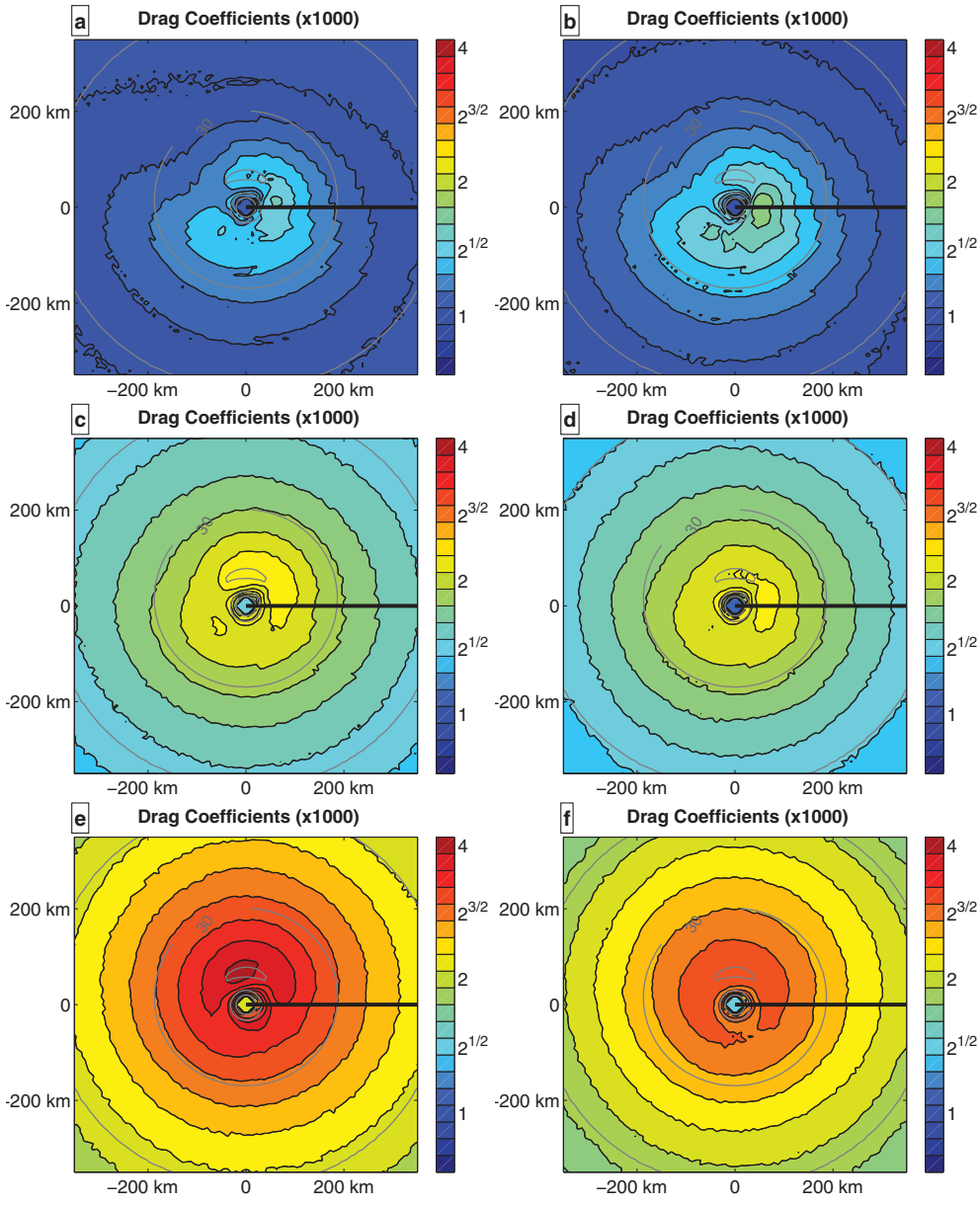

Figure 5. Drag coefficients (× 1000) for a 5 m/s translating tropical cyclone. (a, c, and e) The left column is calculated using the RHG method, while (b, d, and f) the right column is calculated using the DCCM method. The saturation level is B = 0.002 (Figures 5a and 5b), B = 0.006 (Figures 5c and 5d), and B = 0.012 (Figures 5e and 5f). The thick black line represents the track of the tropical cyclone through the domain and the thin gray contours represent 15, 30, and 45 m/s wind speeds.

of the high-frequency tail is enhanced due to breaking, their effect can be accounted for by slightly raising the B value without modifying the approach. In DCCM, the growth rate coefficients have been determined to match observations in the North Sea and under hurricane conditions. Therefore, their coefficients should represent the mean impact of both breaking and nonbreaking waves.

[34] The calculation of the wind profile between the two methods is another major difference. The method of DCCM does not explicitly consider energy conservation in the wave boundary layer, and assumes the wind profile to follow a logarithmic law of the wall profile. There is a feedback on the surface roughness due to the form drag, but the directions of the wind is fixed (in z), that is, the direction of the wind shear is fixed and it can be misaligned with the wind stress direction (which is also constant in z) at all heights. This has a significant effect on the stress calculation, particularly when wind and waves are misaligned. The method of RHG considers energy conservation inside the wave boundary layer. It also assumes that the wind shear and the turbulent stress are aligned at all heights. Therefore, the wind speed vector can turn (change directions) with height inside the wave boundary layer. Since the wind shear and the wind stress are aligned above the

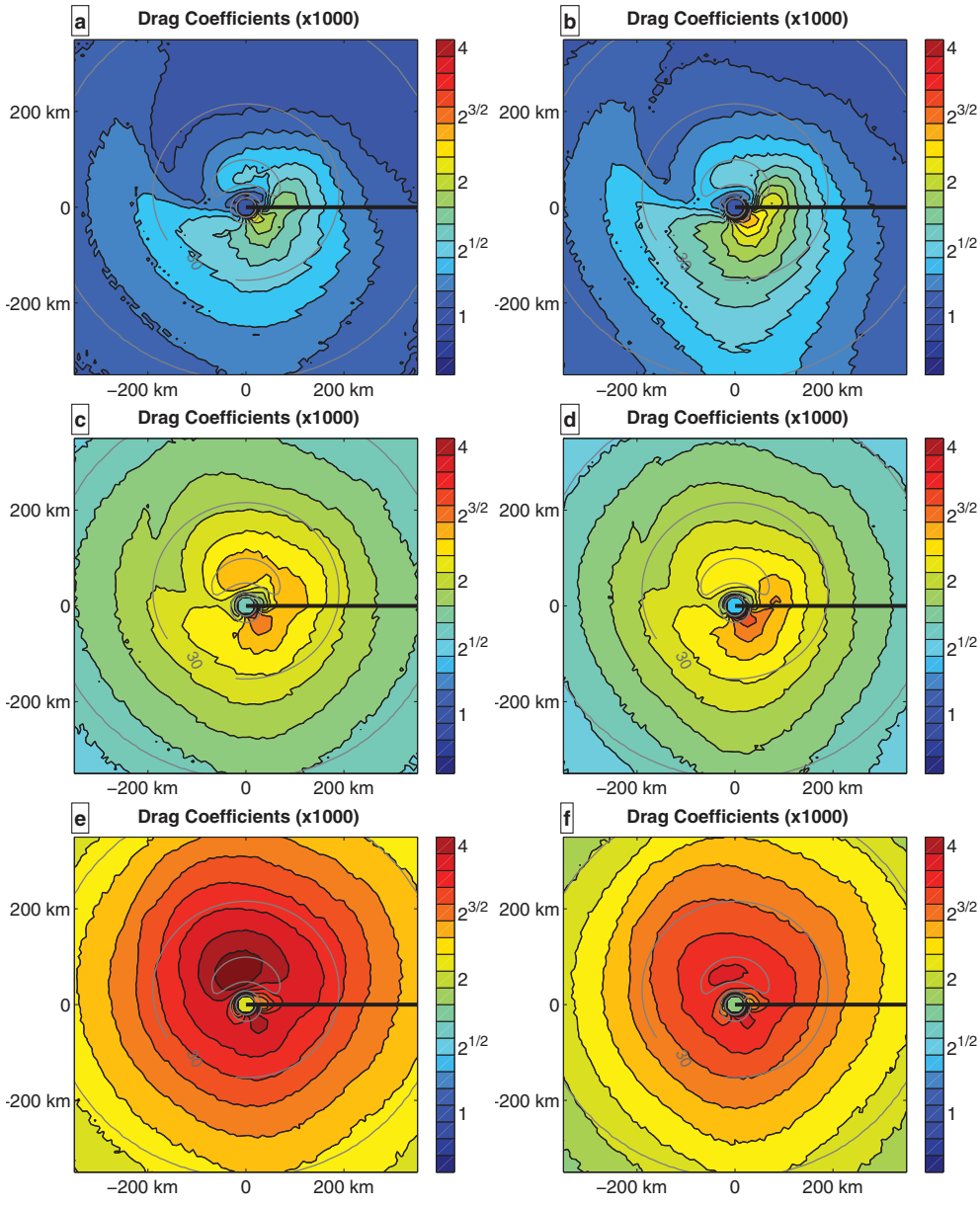

Figure 6. The same as Figure 5, but for a 10 m/s translating tropical cyclone.

wave boundary layer, misalignment between the wind direction and the wind stress direction (if it exists at the top of the wave boundary layer) decreases with height. As shown later, this explicit calculation of the wind profile leads to misalignment angles at 10 m that are about half as large as those at the top of the wave boundary layer.

2.3. Experimental Design

[35] We conduct two numerical experiments. The first experiment is a fetch-dependent simulation under a stationary and uniform wind over a large computational domain. The second experiment is an idealized tropical cyclone that is translated across a computational domain at a fixed speed.

2.3.1. Experiment A: Fetch-Dependent Simulation

[36] The domain is 3000 km in the direction of the wind and 1800 km in the direction normal to the wind. The depth is uniformly 4 km at all locations to maintain deep-water conditions. The wave simulation is run for 72 h so that the wave field reaches a steady state. The wind stress is calculated along the central transect in the wind direction where the fetch increases with distance. The experiment is conducted for wind speeds ranging from 5 to 50 m/s in increments of 5 m/s. We present data up to 400 km fetch, since the effective fetch under strong wind usually does not exceed a few hundred kilometers in typical tropical cyclone conditions.

2.3.2. Experiment B: Idealized Tropical Cyclone Simulation

[37] The second experiment is an idealized tropical cyclone simulation where an axisymmetric tropical cyclone with the *Holland* [1980] wind profile is translated across the same deep-water domain described in Experiment A. The storm is prescribed with a radius of maximum wind of 70 km and a maximum wind speed of 45 m/s. It translates

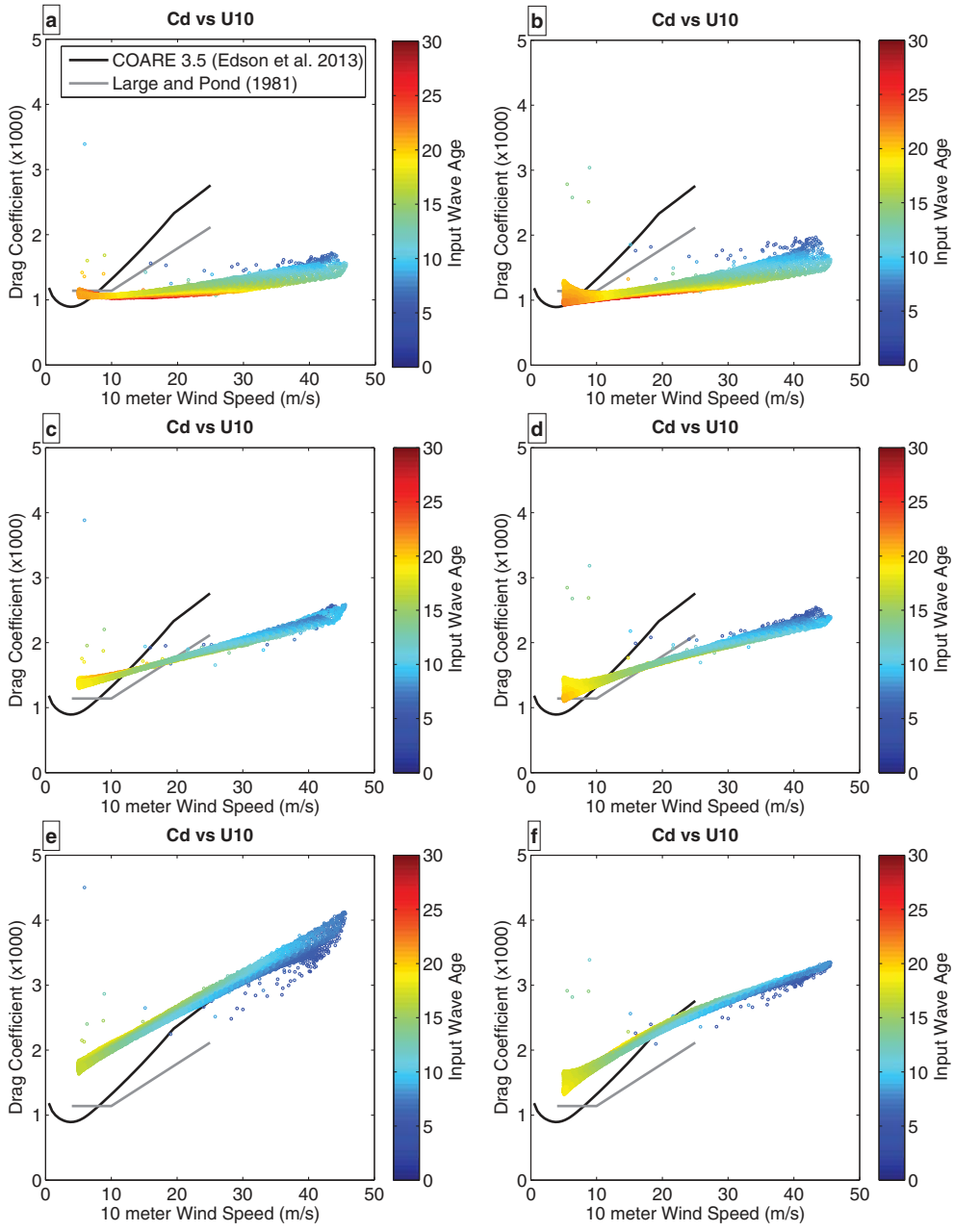

Figure 7. Drag coefficient (× 1000) versus wind speed for a 5 m/s translating tropical cyclone. (a, c, and e) The left column is calculated using the RHG method, while (b, d, and f) the right column is calculated using the DCCM method. The saturation level is B = 0.002 (Figures 7a and 7b), B = 0.006 (Figures 7c and 7d), and B = 0.012 (Figures 7e and 7f).

through the domain for 72 h so that the wave field becomes steady state in the reference frame of the translating storm. The wind and resulting wave field for a 5 and a 10 m/s translating storm are shown in Figure 3. The front right of the storm is exposed to prolonged forcing from wind that produces higher, longer, and older waves because the swell field propagates with the storm (resonance effect). The rear left side of the storm generally produces lower, shorter, and younger waves where the swell, wind, and translating storm vectors can be significantly misaligned. Swell generated some time earlier in the front right quadrant of the storm propagates into the left half of the storm at later times and creates conditions of large misalignment between the swell field and the wind direction. The point where the swell intersects the moving storm varies depending on the translation speed of the storm. All these features have been documented in the previous observational studies [see *Young*, 2003].

3. Results

3.1. Experiment A (Fetch Dependent)

[38] The drag coefficients calculated in the fetch-dependent experiment are presented in Figure 4. The results using RHG are shown in the left column and those using

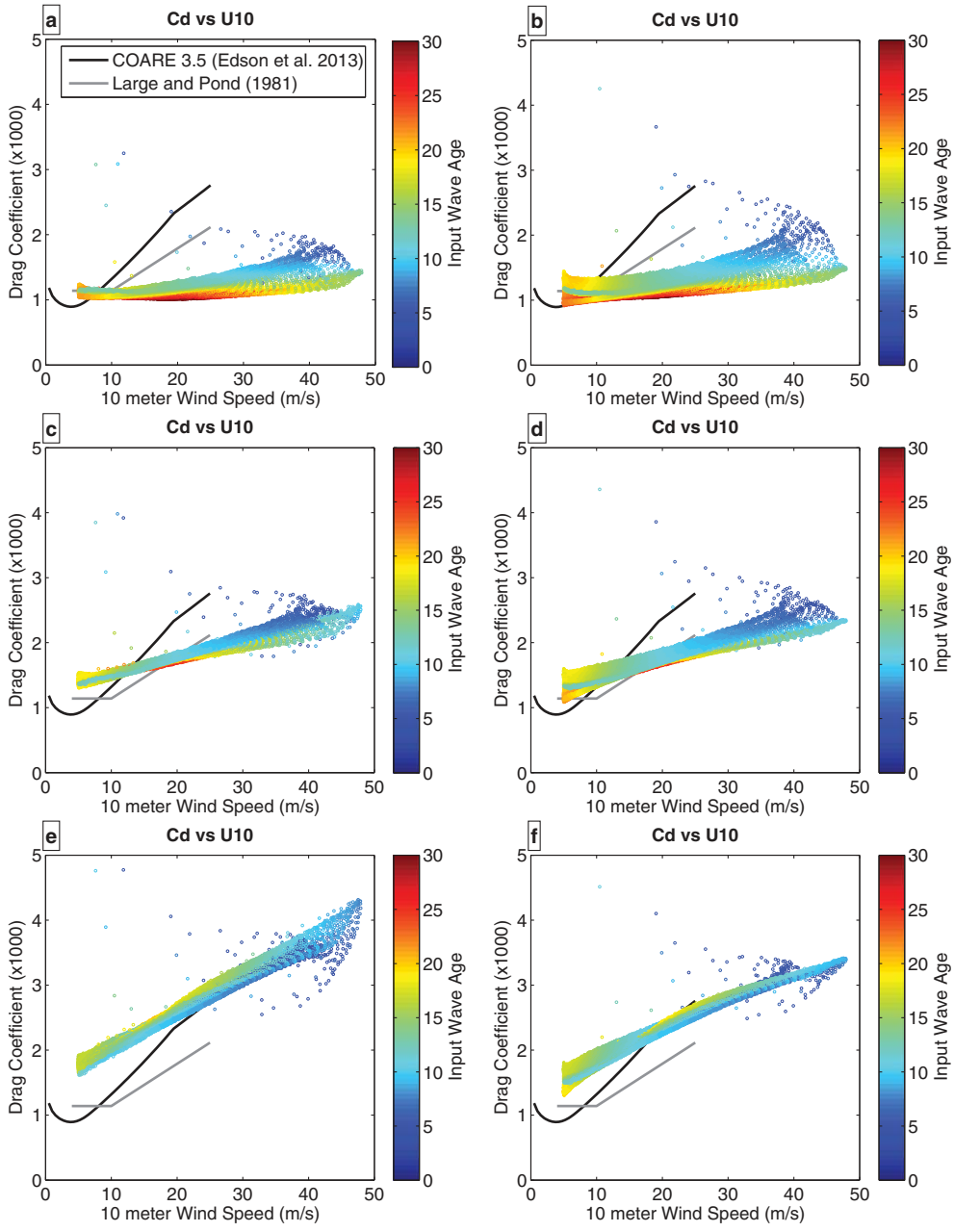

Figure 8. The same as Figure 7, but for a 10 m/s translating tropical cyclone.

DCCM in the right column. The overall results show that the drag coefficient is very sensitive to the choice of the saturation level in the tail and that it is not as sensitive to the different approaches of the drag coefficient calculation (i.e., between RHG and DCCM). As discussed earlier, if the saturation level B is fixed, neither approach reproduces the COARE 3.5 trend from 5 to 25 m/s. At low (5 m/s) winds, the lowest tail level ($B=2\times10^{-3}$) yields the most consistent drag coefficient, but at high (25 m/s) winds the highest tail level ($B=12\times10^{-3}$) yields the values closest to the COARE 3.5 drag coefficient. It is interesting to note that the middle level ($B=6\times10^{-3}$) seems to yield the drag coefficient trend that is consistent with *Large and Pond* [1981] parameterization from 5 to 18 m/s. In all cases the drag coefficient continues to increase with the wind speed if the tail level is kept unchanged. This suggests that the drag coefficient can saturate (cease to increase) or decrease with increasing wind if the tail level decreases with increasing wind. One noticeable difference between RHG and DCCM is that the DCCM drag coefficient is smaller for the highest wind speeds with the highest tail level. This is an indication that RHG drag coefficient is more sensitive to the tail level.

[39] Let us next focus on the sea state dependence of the drag coefficient. The sea state dependence of the drag coefficient is displayed by color coding the data in terms of the input wave age ($c_{pi}/u_{\star}$, where c_{pi} is the phase speed at the wind-sea peak frequency). At a fixed wind speed the drag coefficient varies as the fetch increases from 50 to 400 km. The most significant dependence is observed with DCCM at the highest wind speed and the lowest saturation value

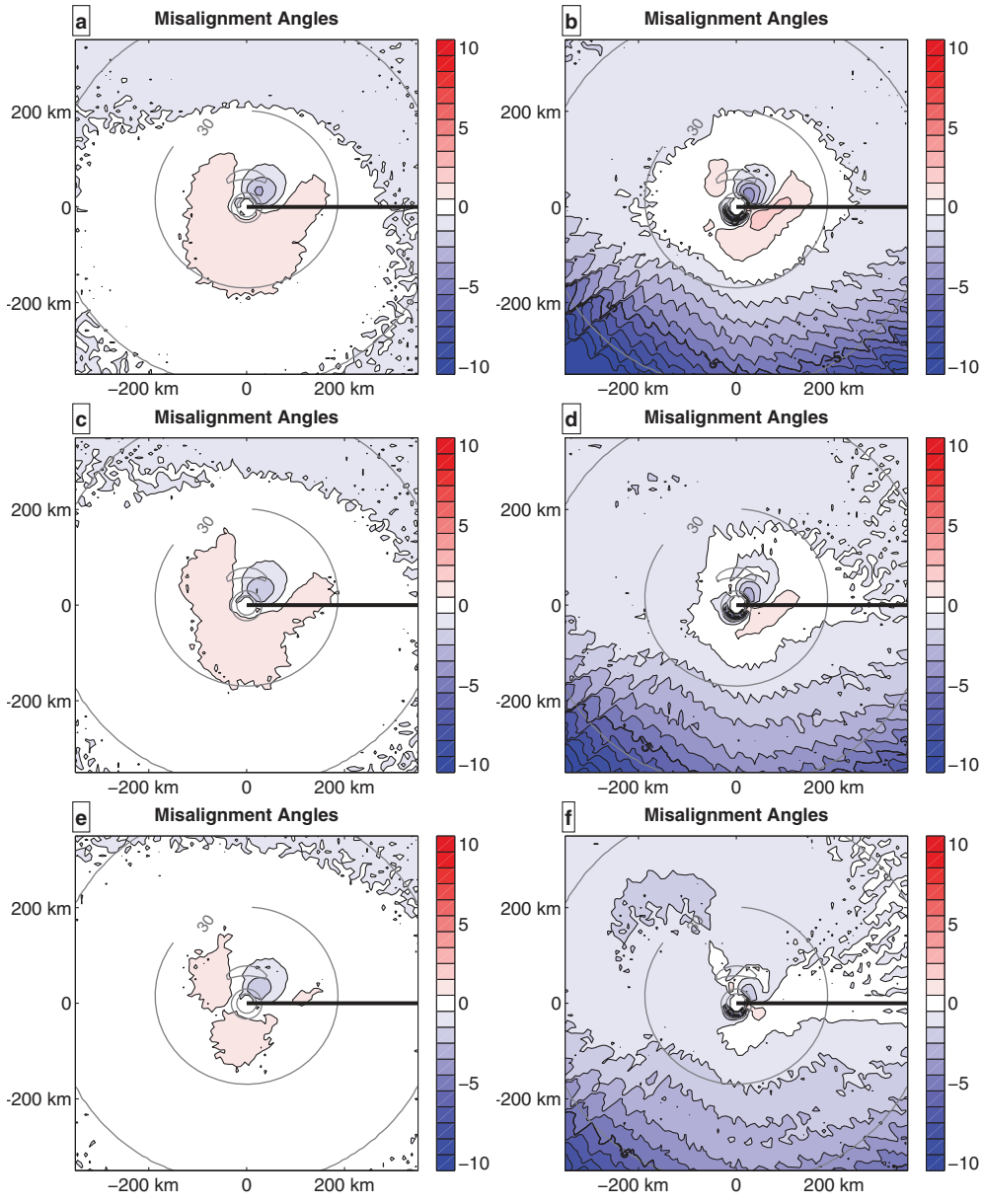

Figure 9. Misalignment angles (10 m wind direction − surface stress direction) for a 5 m/s translating tropical cyclone. (a, c, and e) The left column is calculated using the RHG method, while (b, d, and f) the right column is calculated using the DCCM method. The saturation level is B = 0.002 (Figures 9a and 9b), B = 0.006 (Figures 9c and 9d), and B = 0.012 (Figures 9e and 9f). The thick black line represents the track of the tropical cyclone through the domain and the thin gray contours represent 15, 30, and 45 m/s wind speeds.

($B=2\times10^{-3}$), where the drag coefficient decreases by about 50% as the sea develops. As the tail level increases, the DCCM results show less wave age dependence. With RHG the sea state dependence is not as large with the lowest saturation level ($B=2\times10^{-3}$). Interestingly, as the tail level increases, the sea state dependence (input wave age) reverses; the older seas yield larger drag coefficients with the highest saturation level ($B=12\times10^{-3}$). This reversal happens because the older waves have lower peak input frequencies. As explained earlier, the wave spectrum transitions from the explicit model result to the parameterized tail between 1.25 × and 3 × the peak input frequency. Therefore, older waves adjust to the tail level at a lower frequency. This means that the drag coefficient of older waves is more dependent on the tail level and less dependent on the spectral peak. Thus, with a high tail level (at the same wind speed) the older waves yield higher drag coefficient values. Conversely, when attaching a low tail level, the older waves yield lower drag coefficient values.

3.2. Experiment B (Idealized Tropical Cyclone)

[40] The tropical cyclone experiments contain wave fields where the swell and wind vector are no longer aligned leading to more complex solutions. The calculated

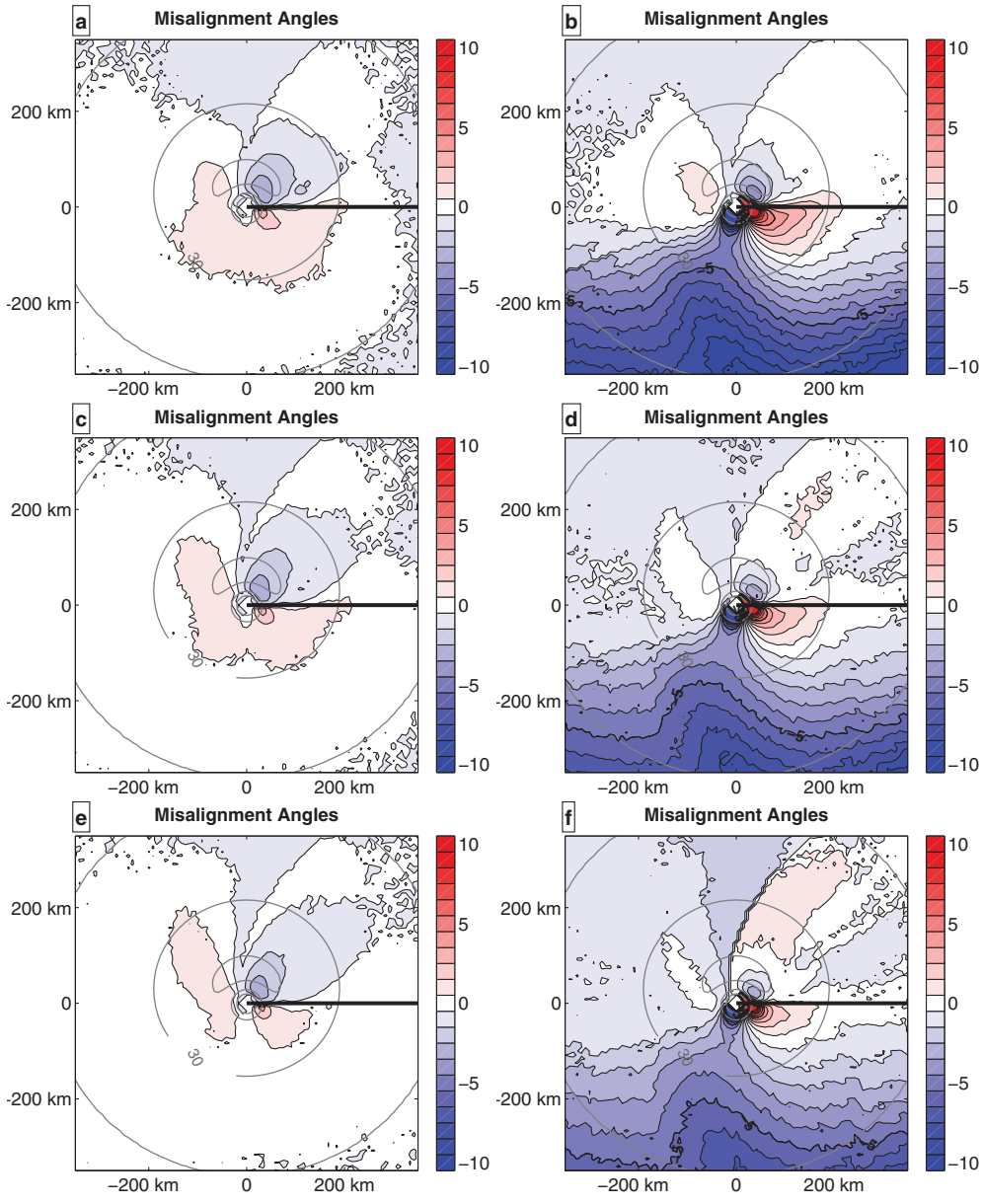

Figure 10. The same as Figure 9, but for a 10 m/s translating tropical cyclone.

angle between the wind vector and the wind stress vector is an important result from these simulations. In general, the largest waves are seen on the right front side of the tropical cyclone where the storm translation speed, wind vector, and wave direction are all in the same direction. The youngest seas are found in the rear and left of the storm where the wind and translation direction are against each other, and the dominant wave direction can be highly misaligned. Note that even if the 10 m wind vector and the wind stress vector are misaligned, we have calculated the drag coefficient as a ratio of the friction velocity squared and the 10 m wind speed squared.

[41] As in Experiment A, the drag coefficient value is overall very sensitive to the tail level attached and is not as sensitive to the approaches of the stress calculation (Figures 5–8). The sea state dependence of the drag coefficient for a 5 m/s translating tropical cyclone is comparable to that for growing seas in Experiment A, but it is significantly enhanced when the translation speed increases from 5 m/s (Figures 5 and 7) to 10 m/s (Figures 6 and 8). The largest increase in sea state dependence occurs with the lowest tail level. Specifically, as the translation speed increases from 5 to 10 m/s, the range of drag coefficient at wind speed 40 m/s increases from roughly $1.3-1.6\times10^{-3}$ to $1.1-2\times10^{-3}$ in RHG, and from $1.4-1.9\times10^{-3}$ to $1.2-2.3\times10^{-3}$ in DCCM. This is mainly because waves that propagate against the wind (counter swell) on the rear left of the storm center have a notable impact inside the radius of maximum wind. The presence of such a region is strongly dependent on the translation of the storm and the propagation of the swell. The counter-swell effect is not as strong with the 5 m/s translating storm because the swell field does not intersect the storm track at the same location. This sensitivity of the swell field to the translation speed is

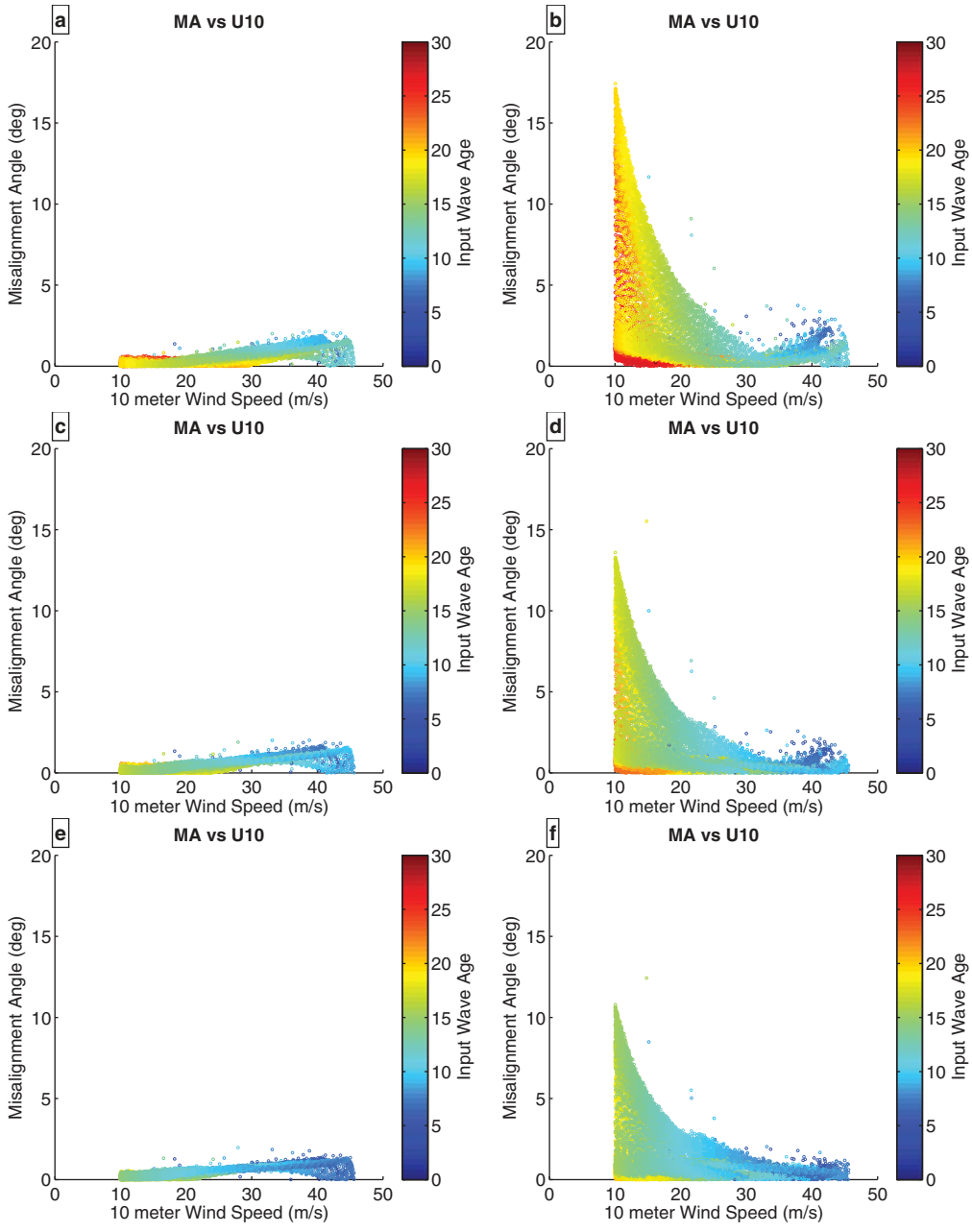

Figure 11. Misalignment angle (10 m wind direction − surface stress direction) versus wind speed for a 5 m/s translating tropical cyclone. (a, c, and e) The left column is calculated using the RHG method, while (b, d, and f) the right column is calculated using the DCCM method. The saturation level is B = 0.002 (Figures 11a and 11b), B = 0.006 (Figures 11c and 11d), and B = 0.012 (Figures 11e and 11f).

consistent with the modeling results of *Moon et al*. [2003]. The effect of the counter swell is more pronounced in the results of DCCM than those of RHG. Consequently, the location of the maximum drag coefficient moves further to the rear right in the DCCM results (Figures 5 and 6).

[42] We next examine the misalignment angle between the 10 m wind speed vector and the wind stress vector (Figures 9–12). There are significant differences between the RHG results and the DCCM results. The misalignment angle is generally small (up to a few degrees) in the RHG results, but it is significantly larger (exceeding 5° very close to the storm center as well as very far from the storm center) in the DCCM results. The misalignment is more enhanced when the wind speed is lower (right plots of Figures 11 and 12). The misalignment is also enhanced to the left of the storm (Figures 9 and 10, right) likely because misaligned swell is present there.

[43] The significant difference of the wind stress misalignment angle predictions between RHG and DCCM is caused by two major differences in the two methods. The first difference is in the estimations of the mean wind profile. As discussed earlier, DCCM assumes that the wind direction does not change with height. Therefore, the misalignment angle between the wind and wind stress is also

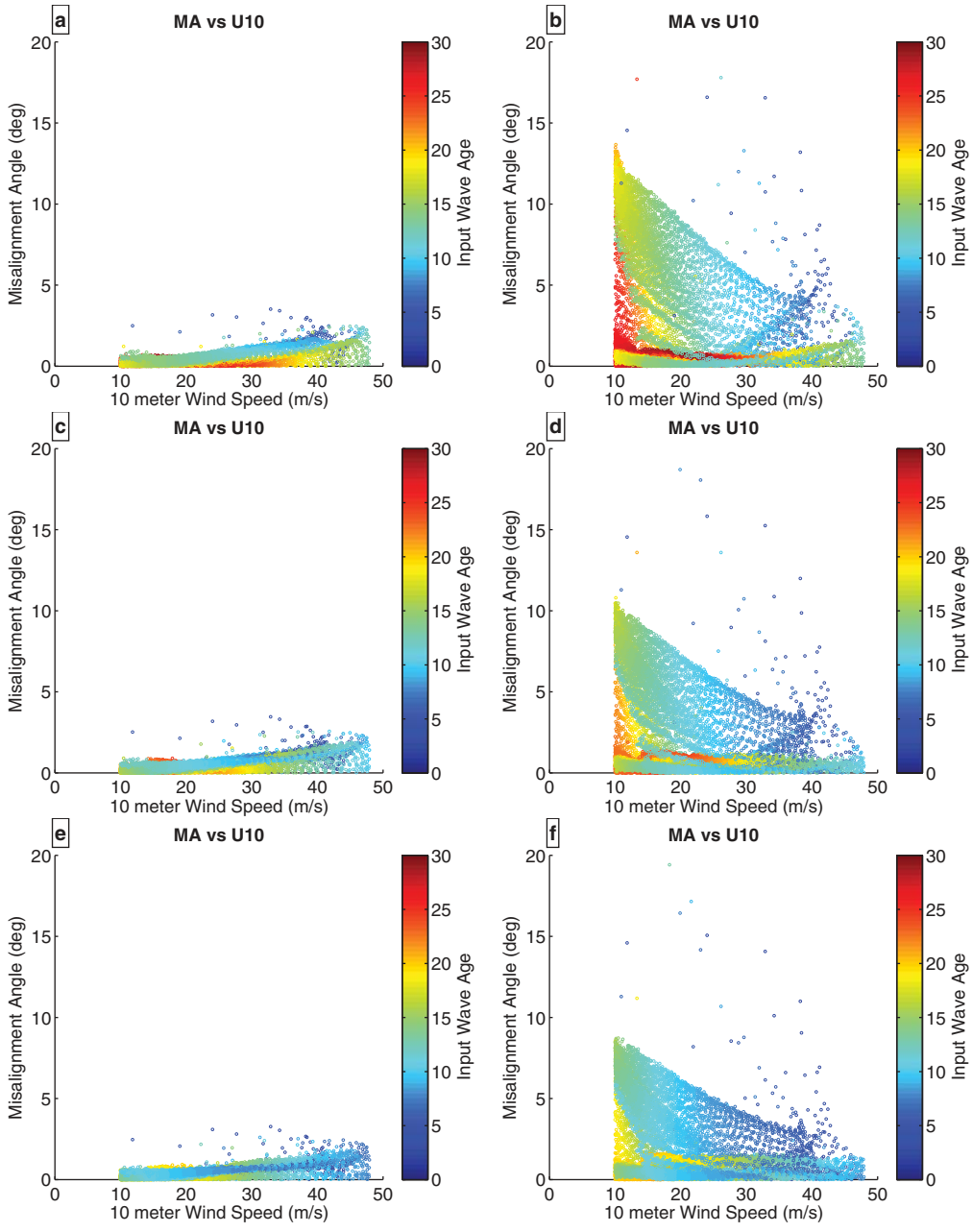

Figure 12. The same as Figure 11, but for a 10 m/s translating tropical cyclone.

independent of height (at least up to 10 m height). However, RHG imposes that the wind shear is in the same direction as the turbulent stress at all heights. Consequently, above the top of the wave boundary layer (outside the direct wave effects) the wind shear is aligned with the wind stress, that is, the misalignment angle decreases with height. In fact, we have found that the misalignment angle is typically about half at 10 m height compared to that at the top of the wave boundary layer (which is typically 1.5 m).

[44] The second and more significant difference between RHG and DCCM is the directionality of the growth rate and the impacts of cross-wind swell. Because the growth rate of RHG has a cosine squared dependence on the angle between the wind stress and the waves, cross-wind swell has essentially no impact. DCCM calculates the growth rate based on the difference between the wind speed projected in the wave direction and the wave phase speed (from equation (3)). If the wind and waves are misaligned by around 90° the growth rate approaches

$$\beta_g(k,\theta) \rightarrow A_1 \sigma \frac{-(c^2)}{c^2} \frac{\rho_a}{\rho_w} \tag{19}$$

instead of 0. In particular, if the misalignment is slightly larger than 90°, the coefficient A_1 is as large as that for the strongly forced wind seas (see equation (4)). Since the form drag of the cross-wind swell applies in the direction of the swell (perpendicular to the wind direction), these

waves are very effective in turning the wind stress direction. (Note that swell that propagates against the wind may increase the wind stress and the drag coefficient but it does not turn the wind stress direction.)

[45] There are a few previous studies addressing the misalignment between the 10 m wind vector and the wind stress vector [*Geernaert*, 1988; *Drennan et al*., 1999; *Grachev et al*., 2003; *Zhang et al*., 2009]. While most of these studies only demonstrated statistically significant misalignment at low wind speeds (<5 m/s) [*Geernaert*, 1988; *Drennan et al*., 1999; *Grachev et al*., 2003], recent observations by *Zhang et al*. [2009] suggest that certain conditions (such as the presence of strong horizontal current shears that can turn waves near the peak) can result in stress angles misaligned by more than 20° from the wind direction for wind speeds up to 15 m/s. These results have not been observed over a wide range of wave conditions, so their implications for hurricane conditions are not clear. Therefore, it is difficult to validate our model results against existing observations. Nevertheless, this study clarifies how different assumptions in the drag coefficient calculations yield very different results of the wind stress misalignment.

[46] Several studies have attempted to observe the drag coefficient under tropical cyclones [*Powell et al*., 2003; *Black et al*., 2007; *French et al*., 2007; *Jarosz et al*., 2007; *Holthuijsen et al*., 2012]. *Holthuijsen et al*. [2012] reports drag coefficients for 20 m/s winds that are about 1×10^{-3}, which is much lower than the COARE 3.5 algorithm [*Edson et al*., 2013] (2.4×10^{-3}) and *Large and Pond* [1981] (1.79×10^{-3}). Results from the other studies [*Powell et al*., 2003; *Black et al*., 2007; *French et al*., 2007; *Jarosz et al*., 2007] show mean values at 20 m/s more comparable to the values of *Large and Pond* [1981] but are still lower than the COARE 3.5 algorithm. At higher wind speeds the observational studies generally agree that the drag coefficient saturates or is reduced, but the wind speed at which this saturation/reduction occurs is variable (30–50 m/s). As mentioned previously our model results do not show saturation/reduction of the drag coefficient in either method unless the tail level is reduced with increasing wind speed.

[47] A couple of studies [*Black et al*., 2007; *Holthuijsen et al*., 2012] have explored the dependence of the drag coefficient based on the location relative to the storm translation. *Black et al*. [2007] presented observations from three of the four tropical cyclone quadrants and saw no systematic dependence of the drag coefficient. *Holthuijsen et al*. [2012], however, found a strong dependence of the drag coefficient on the location relative to the storm track. They classified their observations into three regions (left-front third, right-front third, and rear third, relative to the storm center). The results suggest that at wind speed about 20 m/s the drag coefficient varies from 0.7×10^{-3} in the left-front third to 1.3×10^{-3} in the rear third. Their results at wind speed about 35 m/s show the drag coefficient varies from about 1.8×10^{-3} in the right-front third to 5.2×10^{-3} in the left-front third, a difference of almost 300%. In our model calculations, if the tail level is fixed or is a function of wind speed only, the variability of the drag coefficient at a fixed wind speed is at most 50–100%. Even if B is allowed to be sea state dependent, it is not likely that the model results yield such large systematic variations of the drag coefficient as seen by *Holthuijsen et al*. [2012]. They have attributed the large variability to the presence of cross-wind swells and counter swells. Although our model results show some sensitivity of the drag coefficient to cross-wind and counter swells, the impact of swell is never as large as the study of *Holthuijsen et al*. [2012] suggests. Furthermore, for wind speeds up to 25 m/s the model results predict that cross-wind swell and counter swell tend to increase the drag coefficient, which is opposite to the trend reported by *Holthuijsen et al*. [2012]. The increase in the drag coefficient due to cross swell for wind speeds 25–45 m/s in our model results is much less than the increase reported by *Holthuijsen et al*. [2012].

4. Conclusion

[48] The sea state dependence of the air-sea momentum flux and the drag coefficient was studied with simple fetch-dependent wave fields under uniform wind and with complex wave fields under hurricane wind conditions. Two very different approaches (RHG and DCCM) were used to calculate the wind stress and the mean wind profile. Using existing observations as guidance, a range of spectral saturation levels at high frequencies (spectral tail) were tested in the wind stress calculations.

[49] The most important finding of this study is that the drag coefficient is very sensitive to the spectral saturation level but is not as sensitive to the wind stress calculation approaches. If the saturation level is taken to be a function of wind speed, wave age, or both, then the drag coefficient can be constructed to match any observations or empirical parameterizations. This result supports the conclusion of *Makin et al*. [1995] and others that the waves between

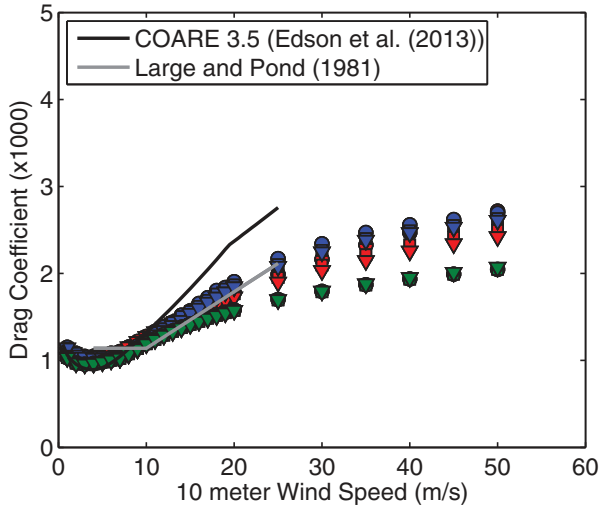

Figure A1. Drag coefficients (×1000) calculated using the three different methods with the empirical spectrum of *Elfouhaily et al*. [1997]. The red symbols are values calculated using the RHG method, the green symbols are values calculated using the DCCM method, and the blue symbols are values calculated using the *Mueller and Veron* [2009] method. The triangles are calculated at a fetch of 10 km, the squares at a fetch of 100 km, and the circles are from fully developed (infinite fetch) spectrum.

centimeters to meters scale have significant contributions to the air-sea momentum flux. If the spectral saturation level is assumed to remain constant at higher wind speeds, the drag coefficient continues to increase with increasing wind. Saturation or reduction of the drag coefficient at very high wind speeds occurs only if the saturation level decreases with increasing wind speed within the framework of our model study. It is possible that presence of sea sprays and sea foam, which is not considered in this study, may contribute to reducing the drag coefficient at very high wind speeds. Airflow separation, as discussed in *Donelan et al*. [2006] may also play a role in the reduction/modification of the drag.

[50] Although both RHG and DCCM methods yield similar drag coefficient values, the results of the misalignment angle between the 10 m wind speed vector and the wind stress vector in the tropical cyclone experiments are very different between the two methods. While the wind stress-based growth rate parameterization of RHG prevents cross-wind swell (waves that are propagating perpendicular to the wind) from having a large impact on the wind stress, the wind speed-based growth rate parameterization of

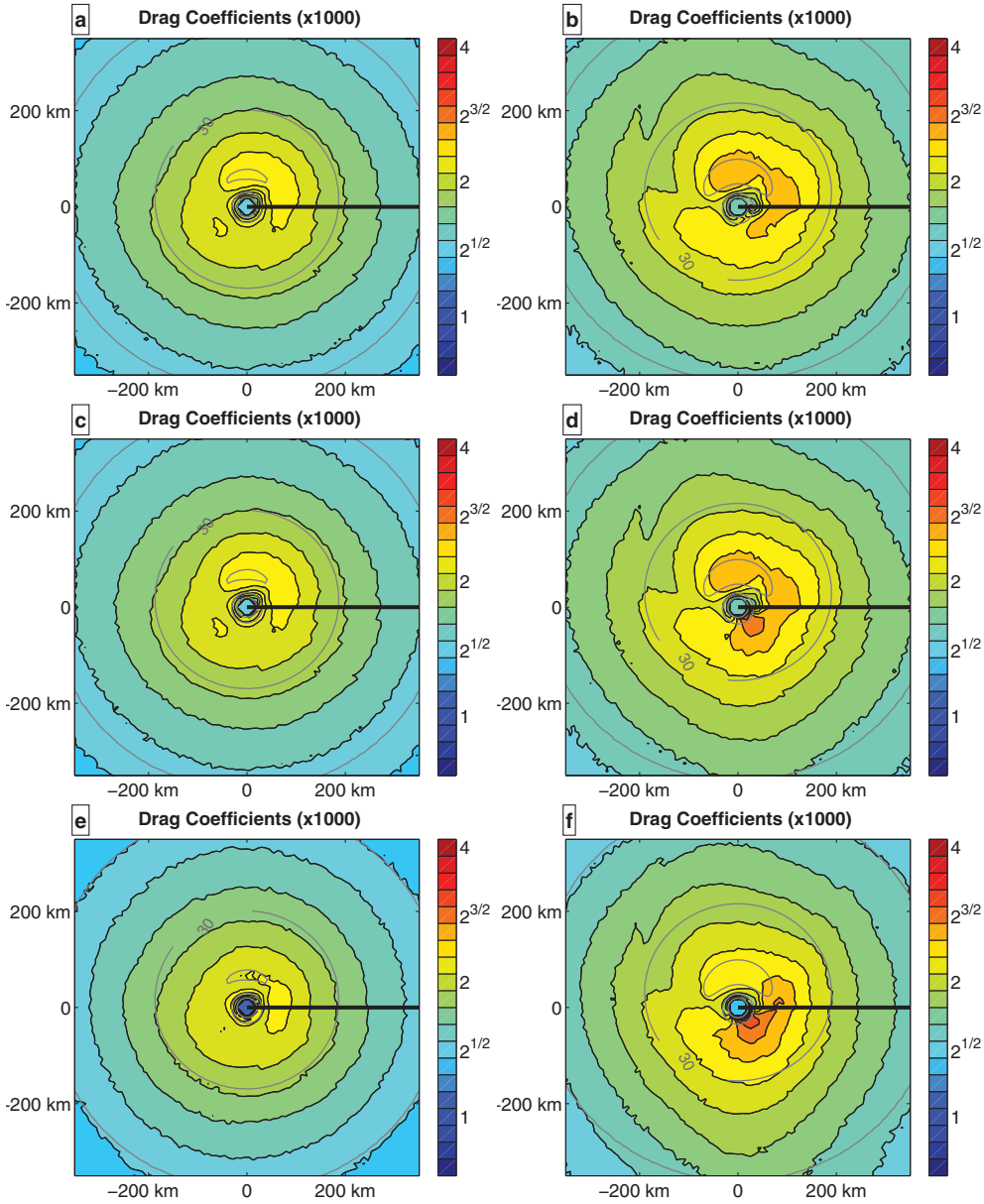

Figure B1. Drag coefficients (× 1000) for a (a, c, and e) 5 m/s and (b, d, and f) 10 m/s translating tropical cyclone with saturation level B = 0.006. The RHG drag coefficient with the growth rate of the counter swell equal to 40% of the growth rate for wind sea (Figures B1a and B1b), the RHG drag coefficient with the growth rate of the counter swell equal to that of the wind sea (Figures B1c and B1d), and DCCM drag coefficient (Figures B1e and B1f). The thick black line represents tropical cyclone's track through the domain and the thin gray contours represent 15, 30, and 45 m/s wind speeds.

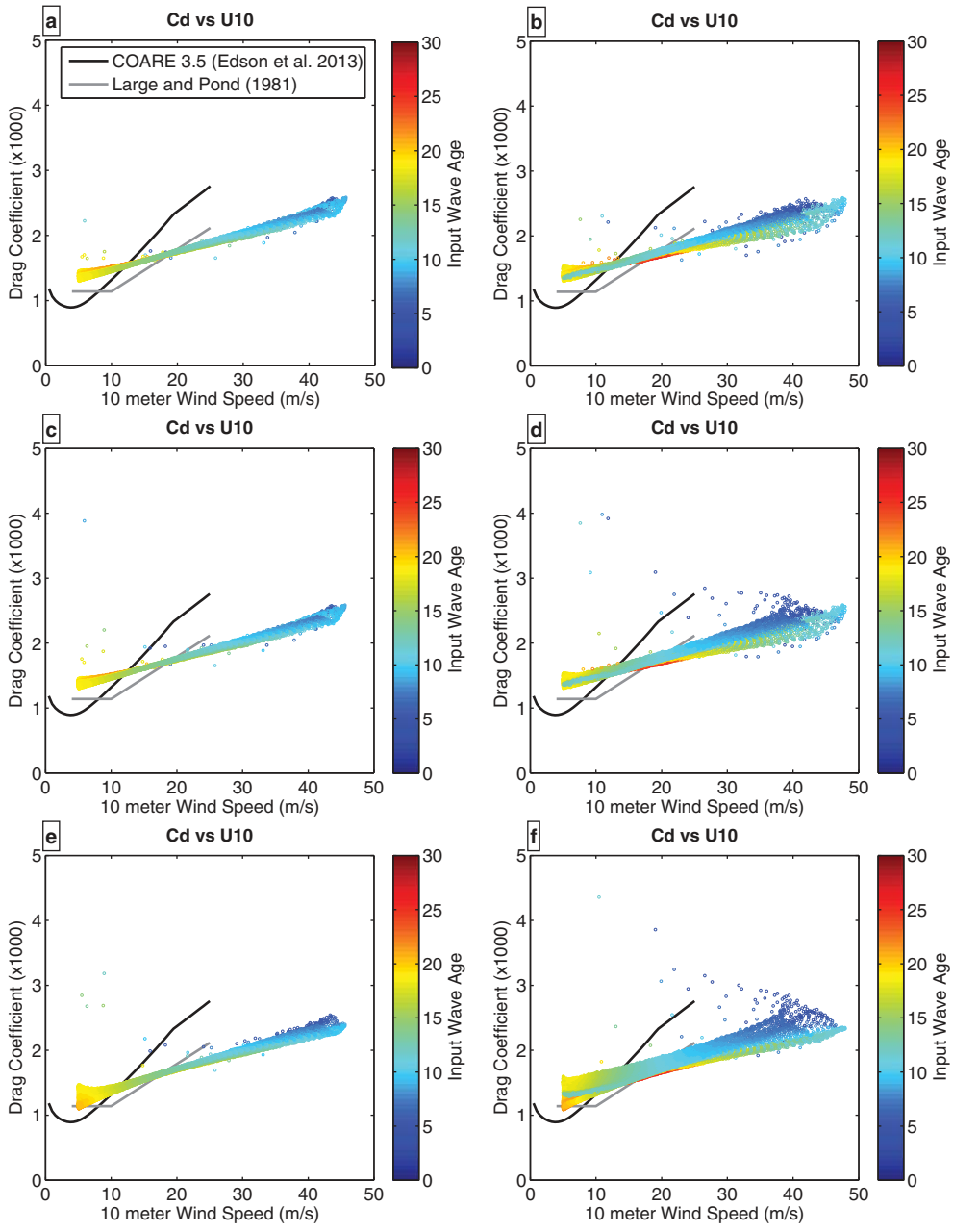

Figure B2. The same as Figure B1, but for drag coefficient (× 1000) versus wind speed.

DCCM introduces a significant contribution from cross-wind swell to the wind stress and increases the misalignment of the wind stress vector and wind speed vector. (The stress supported by cross swell does not significantly alter the wind stress magnitude, but modifies the wind stress direction.) The 10 m/s translation speed tropical cyclone consistently gives more misalignment than the 5 m/s translating tropical cyclone.

[51] The sea state dependence of the drag coefficient is sensitive to the tail level. In particular, with the RHG method the dependence of the drag coefficient on the wave age reverses as the tail level increase from the lowest level to the highest level studied. The results also show that the fetch-dependent seas and the 5 m/s translating tropical cyclone give comparable sea state dependence, while the 10 m/s translating tropical cyclone yields a much larger sea state dependence. The sea state dependence is enhanced to the left of the storm track, particularly because of the presence of swell that is uncorrelated with the local wind. With the lowest tail level tested ($B=2\times10^{-3}$) both RHG and DCCM show that the drag coefficient can vary by as much as 100% at wind speed 40 m/s for a 10 m/s translation speed tropical cyclone. More typically, our results show variability of the drag coefficient less than 50% at a given wind speed for a fixed tail level.

[52] Our modeling results (both RHG and DCCM) are generally not consistent with the observational study of *Holthuijsen et al.* [2012]. The magnitude of the sea state dependence of our models is significantly smaller than that reported by *Holthuijsen et al.* [2012]. Furthermore, for

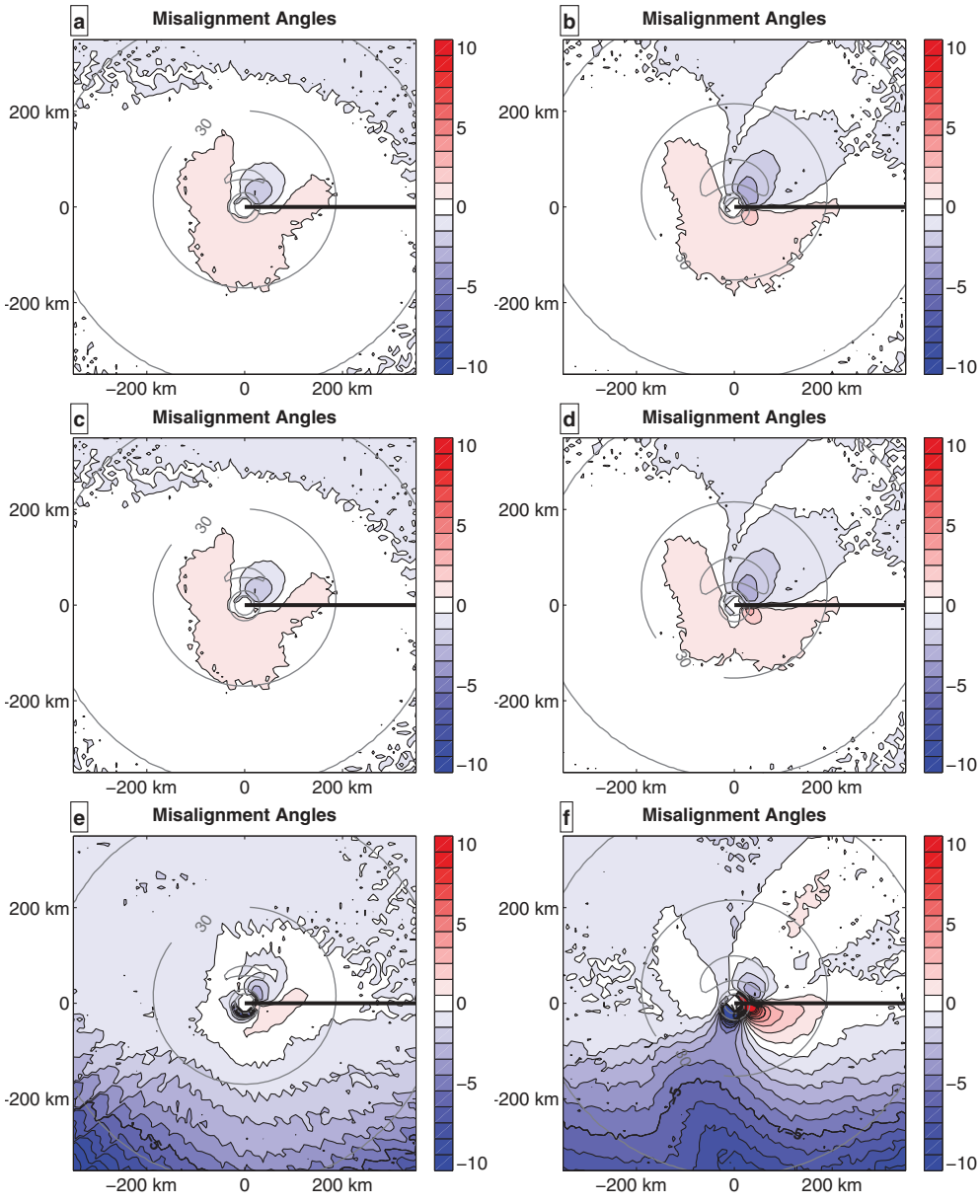

Figure B3. The same as Figure B1, but for misalignment angle (10 m wind direction − surface stress direction).

wind speeds up to 25 m/s, the model results predict that cross-wind swell and counter swell tend to increase the drag coefficient, which is opposite to the trend reported by *Holthuijsen et al*. [2012]. The increase in the drag coefficient due to cross swell for wind speeds 25–45 m/s in the model results is much less than the increase reported by *Holthuijsen et al*. [2012].

[53] The impact of sea state-dependent air-sea momentum flux and the drag coefficient (including the misalignment between wind and wind stress) will likely have an impact on the upper ocean mixing and resulting sea surface cooling, which will in turn have an impact on the strength of the storm. These impacts can be evaluated more thoroughly with the help of fully coupled atmosphere-wave-ocean models. Because the wind stress also serves as a bottom boundary condition in the atmospheric model, it will likely impact the tropical cyclone dynamics as well.

Appendix A: Wind Stress Calculations With Empirical Wave Spectra and Comparison With Results of *Mueller and Veron* [2009]

[54] It is of interest to apply the well-known empirical wave spectra of *Elfouhaily et al*. [1997] in the two RHG and DCCM approaches to estimate the wave age-dependent drag coefficient. In particular, this allows us to compare another stress calculation approach of *Mueller and Veron* [2009], who included an explicit breaking-wave stress impact and applied the method to the *Elfouhaily et al*. [1997] spectra. In *Mueller and Veron* [2009], the

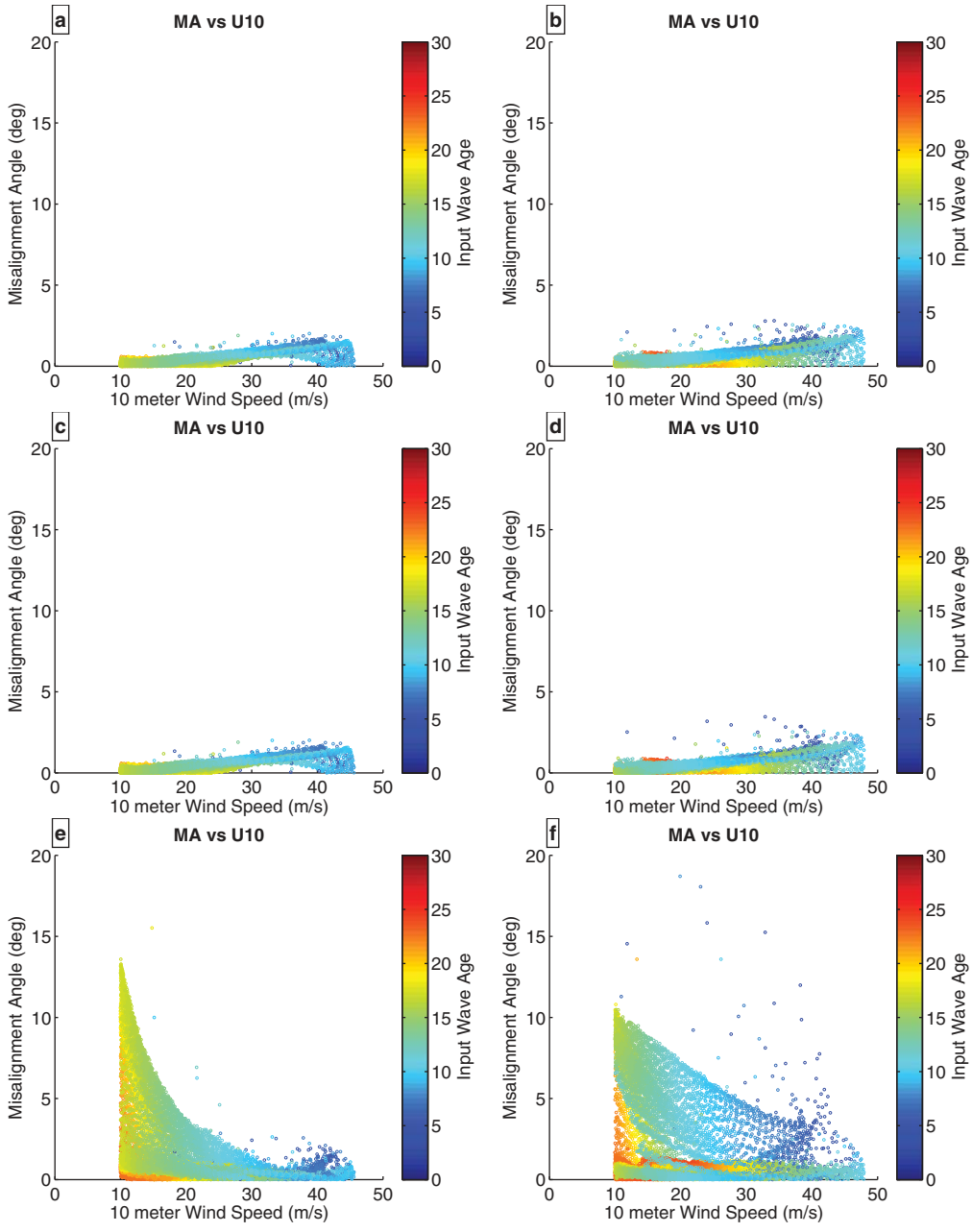

Figure B4. The same as Figure B1, but for misalignment angle (10 m wind direction − surface stress direction) versus wind speed.

stress is given as the sum of the viscous component, the form drag component, and a breaking-wave separation stress component.

$$\tau(z=0)=\tau_v+\tau_w+\tau_s \tag{A1}$$

[55] The growth rate of nonbreaking waves is calculated similarly to RGH. To calculate an explicit breaking-wave stress term, they must infer a breaking-wave distribution. They parameterize their breaking-wave distribution in terms of the saturation spectrum and the growth rate. Ultimately this leads to a calculation of the breaking-wave stress that is similar to the nonbreaking stress calculation. There is also no feedback mechanism considered for the breaking or nonbreaking waveform drag on the mean wind profile.

[56] The results of RHG, DCCM, and the *Mueller and Veron* [2009] methods are shown in Figure A1. The three methods yield a similar trend in the drag coefficient with wind speed. One notable difference between the results with the WW3 wave spectrum and those with the empirical wave spectrum is that the latter tends to saturate (or increase more slowly) at higher wind speeds. This is mainly because the empirical saturation spectrum of *Elfouhaily et al*. [1997] decreases with wind speed beyond the spectral peak and outside the gravity-capillary range. This is consistent with our earlier statement that saturation or reduction of the drag coefficient at high wind speeds can be

realized if the tail level is systematically reduced as wind speed increases.

[57] The method of DCCM yields the lowest drag coefficients at higher wind speeds. This is attributed to the DCCM method being less sensitive to the shortest (highest frequency) waves where the *Elfouhaily et al*. [1997] spectrum can become quite high (see Figure 1). The methods of RHG and *Mueller and Veron* [2009] yield quite similar results at all wind speeds. These results with the empirical tail are generally consistent with our earlier results using WW3 and the parameterized tail, at least in simple fetch-dependent conditions.

Appendix B: Effect of Counter Swell on the Drag Coefficient

[58] Although we have assumed that the counter-swell effect is large in RHG, being consistent with DCCM, the effect of the counter swell is not well understood. In fact, a different growth rate parameterization with a small contribution from the counter swell has been suggested (S. Zieger and A. Babanin, personal communication, 2013). Here, we examine the impact of the counter-swell growth rate on the drag coefficient using the RHG approach, by setting the counter-swell forcing $c_\beta = -10$ instead of -25. The tail level is fixed at the middle level ($B = 6\times10^{-3}$).

[59] The results are shown in Figures B1–B4. Although the 5 m/s translation results (left) show no significant changes (upper and middle images), the 10 m/s translation results (right) show a more noticeable difference on the left of the storm track. The RHG results with a smaller counter-swell coefficient do not contain the large drag coefficient on the inner left-rear of the tropical cyclone seen in the original RHG (middle) and the DCCM (bottom). Figures B1 and B2 also shows that with a large (10 m/s) translation speed the counter swell may significantly increase the sea state dependence of the drag coefficient. However, Figures B3 and B4 show that the misalignment angle between the wind speed vector and the wind stress vector is hardly affected by the counter swell in RHG. This is expected since cross-wind swell has little impact on the drag coefficient in RHG as discussed earlier.

[60] **Acknowledgments.** The authors would like to acknowledge Mark Donelan for his valuable input throughout this project. The authors would also like to acknowledge Hendrik Tolman, Arun Chawla, and J. Henrique Alves for their support related to the work. B. Reichl would like to acknowledge Biju Thomas for his computing assistance. This work was funded by ONR/NOAA NOPP grant N00014-10-1-0154.

References

Banner, M. L., and R. P. Morison (2010), Refined source terms in wind wave models with explicit wave breaking prediction. Part I: Model framework and validation against field data, *Ocean Modell.*, *33*, 177–189, doi:10.1016/j.ocemod.2010.01.002.

Banner, M. L., I. S. F. Jones, and J. C. Trinder (1989), Wavenumber spectra of short gravity waves, *J. Fluid Mech.*, *198*, 321–344, doi:10.1017/S0022112089000157.

Belcher, S. E. (1999), Wave growth by non-separated sheltering, *Eur. J. Mech. B*, *18*, 447–462, doi:10.1016/S0997-7546(99)80041-7.

Black, P. G., E. A. D'Asaro, W. M. Drennan, J. R. French, P. P. Niiler, T. B. Sanford, E. J. Terrill, E. J. Walsh, and J. A. Zhang (2007), Air-sea exchange in hurricanes: Synthesis of observations from the coupled boundary layer air-sea transfer experiment, *Bull. Am. Meteorol. Soc.*, *88*(3), 357–374, doi:10.1175/BAMS-88-3-357.

Cox, C., and W. Munk (1954), Measurement of the roughness of the sea surface from photographs of the sun's glitter, *J. Opt. Soc. Am.*, *44*(11), 838–850, doi:10.1364/JOSA.44.000838.

Donelan, M. A., W. M. Drennan, and K. B. Katsaros (1997), The air-sea momentum flux in conditions of wind sea and swell, *J. Phys. Oceanogr.*, *27*, 2087–2099, doi:10.1175/1520-0485(1997)027<2087:TASMFI>2.0.CO;2.

Donelan, M. A., A. V. Babanin, I. R. Young, and M. L. Banner (2006), Wave-follower field measurements of the wind-input spectral function. Part II: Parameterization of the wind input, *J. Phys. Oceanogr.*, *36*, 1672–1689, doi:10.1175/JTECH1725.1.

Donelan, M. A., M. Curcic, S. S. Chen, and A. K. Magnusson (2012), Modeling waves and wind stress, *J. Geophys. Res.*, *117*, C00J23, doi:10.1029/2011JC007787.

Drennan, W. M., H. C. Graber, and M. A. Donelan (1999), Evidence for the effects of swell and unsteady winds on marine wind stress, *J. Phys. Oceanogr.*, *29*, 1853–1864, doi:10.1175/1520-0485(1999)029<1853:EFTEOS>2.0.CO;2.

Edson, J. B., V. Jampana, R. A. Weller, S. P. Bigorre, A. J. Plueddemann, C. W. Fairall, S. D. Miller, L. Mahrt, D. Vickers, and H. Hersbach (2013), On the exchange of momentum over the open ocean, *J. Phys. Oceanogr.*, *43*, 1589–1610, doi:10.1175/JPO-D-12–0173.1.

Elfouhaily, T., B. Chapron, K. Katsaros, and D. Vandemark (1997), A unified directional spectrum for long and short wind-driven waves, *J. Geophys. Res.*, *102*(C7), 15,781–15,796, doi:10.1029/97JC00467.

Fan, Y., I. Ginis, T. Hara, C. W. Wright, and E. J. Walsh (2009), Numerical simulations and observations of surface wave fields under an extreme tropical cyclone, *J. Phys. Oceanogr.*, *39*, 2097–2116, doi:10.1175/2009JPO4224.1.

Forristall, G. Z. (1981), Measurements of a saturated range in ocean wave spectra, *J. Geophys. Res.*, *86*(C9), 8075–8084, doi:10.1029/JC086iC09p08075.

French, J. R., W. M. Drennan, J. A. Zhang, and P. G. Black (2007), Turbulent fluxes in the hurricane boundary layer. Part I: Momentum flux, *J. Atmos. Sci.*, *64*, 1089–1102, doi:10.1175/JAS3887.1.

García-Nava, H., F. J. Ocampo-Torres, P. Osuna, and M. A. Donelan (2009), Wind stress in the presence of swell under moderate to strong wind conditions, *J. Geophys. Res.*, *114*, C12008, doi:10.1029/2009JC005389.

García-Nava, H., F. J. Ocampo-Torres, P. A. Hwang, and P. Osuna (2012), Reduction of wind stress due to swell at high wind conditions, *J. Geophys. Res.*, *117*, C00J11, doi:10.1029/2011JC007833.

Geernaert, G. L. (1988), Measurements of the angle between the wind vector and wind stress vector in the surface layer over the North Sea, *J. Geophys. Res.*, *93*(C7), 8215–8220, doi:10.1029/JC093iC07p08215.

Grachev, A. A., C. W. Fairall, J. E. Hare, J. B. Edson, and S. D. Miller (2003), Wind stress vector over ocean waves, *J. Phys. Oceanogr.*, *33*, 2408–2429, doi:10.1175/1520-0485(2003)033<2408:WSVOOW>2.0.CO;2.

Hara, T., and S. E. Belcher (2002), Wind forcing in the equilibrium range of wind-wave spectra, *J. Fluid Mech.*, *470*, 223–245, doi:10.1017/S0022112002001945.

Hara, T., and S. E. Belcher (2004), Wind profile and drag coefficient over mature ocean surface wave spectra, *J. Phys. Oceanogr.*, *34*, 2345–2358, doi:10.1175/JPO2633.1.

Holland, G. J. (1980), An analytic model of the wind and pressure profiles in hurricanes, *Mon. Weather Rev.*, *108*, 1212–1218, doi:10.1175/1520-0493(1980)108<1212:AAMOTW>2.0.CO;2.

Holthuijsen, L. H., M. D. Powell, and J. D. Pietrzak (2012), Wind and waves in extreme hurricanes, *J. Geophys. Res.*, *117*, C09003, doi:10.1029/2012JC007983.

Janssen, P. A. E. M. (1991), Quasi-linear theory of wind-wave generation applied to wave forecasting, *J. Phys. Oceanogr.*, *21*, 1631–1642, doi:10.1175/1520-0485(1991)021<1631:QLTOWW>2.0.CO;2.

Jarosz, E., D. A. Mitchell, D. W. Wang, and W. J. Teague (2007), Bottom-up determination of air-sea momentum exchange under a major tropical cyclone, *Science*, *315*, 1707–1709, doi:10.1126/science.1136466.

Kudryavtsev, V. N., and V. K. Makin (2001), The impact of air-flow separation on the drag of the sea surface, *Boundary Layer Meteorol.*, *98*, 155–171, doi:10.1023/A:1018719917275.

Kudryavtsev, V. N., V. K. Makin, and B. Chapron (1999), Coupled sea surface-atmosphere model: 2. Spectrum of short wind waves, *J. Geophys. Res.*, *104*(C4), 7625–7639, doi:10.1029/1999JC900005.

Kudryavtsev, V. N., V. K. Makin, and J. F. Meirink (2001), Simplified model of the air flow above waves, *Boundary Layer Meteorol.*, *100*, 63–90, doi:10.1023/A:1018914113697.

Kukulka, T., and T. Hara (2008a), The effect of breaking waves on a coupled model of wind and ocean surface waves. Part I: Mature seas, *J. Phys. Oceanogr.*, *38*, 2145–2163, doi:10.1175/2008JPO3961.1.

Kukulka, T., and T. Hara (2008b), The effect of breaking waves on a coupled model of wind and ocean surface waves. Part II: Growing seas, *J. Phys. Oceanogr.*, *38*, 2164–2184, doi:10.1175/2008JPO3962.1.

Large, W. G., and S. Pond (1981), Open ocean momentum flux measurements in moderate to strong winds, *J. Phys. Oceanogr.*, *11*, 324–336, doi:10.1175/1520-0485(1981)011<0324:OOMFMI>2.0.CO;2.

Makin, V. K., and V. N. Kudryavtsev (1999), Coupled sea surface-atmosphere model: 1. Wind over waves coupling, *J. Geophys. Res.*, *104*(C4), 7613–7623, doi:10.1029/1999JC900006.

Makin, V. K., and V. N. Kudryavtsev (2002), Impact of dominant waves on sea drag, *Boundary Layer Meteorol.*, *103*, 83–99, doi:10.1023/A:1014591222717.

Makin, V. K., and C. Mastenbroek (1996), Impact of waves on air-sea exchange of sensible heat and momentum, *Boundary Layer Meteorol.*, *79*, 279–300, doi:10.1007/BF00119442.

Makin, V. K., V. N. Kudryavtsev, and C. Mastenbroek (1995), Drag of the sea surface, *Boundary Layer Meteorol.*, *73*, 159–182, doi:10.1007/BF00708935.

Moon, I.-J., I. Ginis, T. Hara, H. L. Tolman, C. W. Wright, and E. J. Walsh (2003), Numerical simulation of sea surface directional wave spectra under hurricane wind forcing, *J. Phys. Oceanogr.*, *33*, 1680–1706, doi:10.1175/2410.1.

Moon, I.-J., I. Ginis, and T. Hara (2004a), Effect of surface waves on air-sea momentum exchange. Part II: Behavior of the drag coefficient under tropical cyclones, *J. Atmos. Sci.*, *61*, 2334–2348, doi:10.1175/1520-0469(2004)061<2334:EOSWOA>2.0.CO;2.

Moon, I.-J., T. Hara, I. Ginis, S. E. Belcher, and H. L. Tolman (2004b), Effect of surface waves on air-sea momentum exchange. Part I: Effect of mature and growing seas, *J. Atmos. Sci.*, *61*(19), 2321–2333, doi:10.1175/1520-0469(2004)061<2321:EOSWOA>2.0.CO;2.

Mueller, J. A., and F. Veron (2009), Nonlinear formulation of the bulk surface stress over breaking waves: Feedback mechanisms from air-flow separation, *Boundary Layer Meteorol.*, *130*, 117–134, doi:10.1007/s10546-008-9334-6.

Plant, W. J. (1982), A relationship between wind stress and wave slope, *J. Geophys. Res.*, *87*(C3), 1961–1967, doi:10.1029/JC087iC03p01961.

Powell, M. D., P. J. Vickery, and T. A. Reinhold (2003), Reduced drag coefficient for high wind speeds in tropical cyclones, *Nature*, *422*, 279–283, doi:10.1038/nature01481.

Romero, L., and W. K. Melville (2010), Airborne observations of fetch-limited waves in the Gulf of Tehauntepec, *J. Phys. Oceanogr.*, *40*, 441–465, doi:10.1175/2009JPO4127.1.

Snyder, R. L., F. W. Dobson, J. A. Elliott, and R. B. Long (1981), Array measurements of atmospheric pressure fluctuations above surface gravity waves, *J. Fluid Mech.*, *102*, 1–59, doi:10.1017/S0022112081002528.

Tolman, H. L. (2009), User manual and system documentation of WAVEWATCH III version 3.14, Tech. Note 276, NOAA/NWS/NCEP/EMC/MMAB, Camp Springs. [Available at http://polar.ncep.noaa.gov/mmab/papers/tn276/MMAB_276.pdf.]

Tsagareli, K. N., A. V. Babanin, D. J. Walker, and I. R. Young (2010), Numerical investigation of spectral evolution of wind waves. Part I: Wind-input source function, *J. Phys. Oceanogr.*, *40*, 656–666, doi:10.1175/2009JPO4345.1.

Young, I. R. (2003), A review of the sea state generated by hurricanes, *Mar. Struct.*, *16*, 201–218, doi:10.1016/S0951-8339(02)00054-0.

Zhang, F. W., W. M. Drennan, B. K. Haus, and H. C. Graber (2009), On wind-wave-current interactions during the Shoaling Waves Experiment, *J. Geophys. Res.*, *114*, C01018, doi:10.1029/2008JC004998.